Research Paper

GEOSPHERE

GEOSPHERE, v. 19, no. 4

https://doi.org/10.1130/GES02621.1

9 figures (2 are oversize); 4 tables; 1 set of supplemental files

CORRESPONDENCE: sean.p.long@wsu.edu

CITATION: Long, S.P., Barba, W.K., McKay, M.P., and Soignard, E., 2023, Thermal architecture of the Salmon River suture zone, Idaho, USA: Implications for the structural evolution of a ductile accretionary complex during arc-continent collision: Geosphere, v. 19, no. 4, p. 1103–1127, https://doi.org/10.1130/GES02621.1.

Science Editor: Andrea Hampel
Associate Editor: Terry L. Pavlis

Received 26 October 2022
Revision received 23 February 2023
Accepted 12 April 2023

Published online 8 June 2023



# Thermal architecture of the Salmon River suture zone, Idaho, USA: Implications for the structural evolution of a ductile accretionary complex during arc-continent collision

**Sean P. Long[1], William K. Barba[1,2], Matthew P. McKay[3], and Emmanuel Soignard[4]**

[1]School of the Environment, Washington State University, Pullman, Washington 99164, USA
[2]Round Mountain Gold Corporation, P.O. Box 480, Round Mountain, Nevada 89045, USA
[3]Department of Geography, Geology and Planning, Missouri State University, Springfield, Missouri 65897, USA
[4]Eyring Materials Center, Arizona State University, Tempe, Arizona 85287, USA

## ABSTRACT

**Documenting the tectono-thermal evolution of the exhumed ductile portions of orogenic systems is critical for interpreting orogen dynamics. Here, we utilize Raman spectroscopy of carbonaceous material thermometry to quantify the thermal architecture of the Salmon River suture zone in west-central Idaho, USA, which records the Cretaceous collision of the Wallowa island arc terrane with North America. We integrate this thermal architecture with published structural interpretations, geochronology, and pressure-temperature-time histories to interpret the evolution of deformation during arc-continent collision in this portion of the North America Cordillera. Mean peak temperatures within four, ~1–3-km-thick, penetratively deformed thrust sheets in the western part of the suture zone decrease moving structurally downward from 652 ± 28 °C (Pollock Mountain thrust sheet), to 577 ± 30 °C (Rapid River thrust sheet), to 426 ± 32 °C (Morrison Ridge thrust sheet), to 358 ± 18 °C (Heavens Gate thrust sheet). These ductile thrust sheets are separated by 100–500-m-thick intervals of inverted temperatures that surround the mapped positions of thrust faults. We interpret the western part of the suture zone as a ductile accretionary complex that records the progressive underplating and top-to-the-west translation of ductile thrust sheets that were derived from the Wallowa terrane during ca. 144–105 Ma collision-related deformation. Accretion of ductile thrust sheets began at ~30–35 km depths and completed at depths of ~10–20 km. Rocks at all structural levels in the suture zone exhibit distributed ductile fabrics, but the inverted thermal gradients that surround the mapped positions of thrust faults suggest that the majority of top-to-the-west displacement was accommodated within 100–500-m-thick, high-strain, thrust-sense ductile shear zones.**

Sean Long https://orcid.org/0000-0001-6548-9394

## 1. INTRODUCTION

Documenting the evolution of deformation within contractional orogenic systems, including the dominant processes of mass transfer, the kinematic components of the strain field, and the space-time framework of key metamorphic and structural events, is an essential prerequisite for interpreting deformation in the context of orogen dynamics (e.g., Dahlstrom, 1969; Price, 1981; Davis et al., 1983; Dahlen, 1990; Beaumont et al., 2001; Kohn, 2014; Yonkee and Weil, 2015). However, this exercise can be challenging within the exhumed ductile portions of orogenic belts, where strain can be heterogeneously partitioned into localized (e.g., displacement within high-strain ductile shear zones) and spatially dispersed (e.g., micro- to meso-scale deformation that produces distributed ductile fabrics) components, which can make kinematic paths difficult to discern (e.g., Ramsay, 1969; Sanderson, 1982; Fossen and Tikoff, 1993; Means, 1994; Mitra, 1994; Goodwin and Tikoff, 2002; Yonkee, 2005). One approach that can effectively complement structural analysis of ductile orogenic belts is the quantification of the orogenic thermal architecture (i.e., the spatial patterns of peak metamorphic temperatures preserved within thrust sheets and across major thrust faults and shear zones). Modeling-based insights into the thermal regimes that arise within collisional orogenic systems (e.g., Henry et al., 1997; Huerta et al., 1998; Beaumont et al., 2004; Dymkova et al., 2016) allow utilizing the thermal architecture of the ductile portion of an orogenic belt, including the spatial extent and magnitudes of intervals of inverted metamorphism, as a valuable tool to help elucidate the distribution of strain and the relative magnitude of displacement on major structures (e.g., Bollinger et al., 2004; Corrie and Kohn, 2011; Long et al., 2016; Grujic et al., 2020).

The Jurassic–Paleogene North American Cordillera, which was constructed as a consequence of east-directed subduction beneath the North American continental plate, has been the source of important models for fold-thrust belts, foreland basins, and terrane accretion that have been exported globally to understand other active and ancient orogens (e.g., Burchfiel and Davis, 1972, 1975; Coney et al., 1980; Price, 1981; Oldow et al., 1989; Allmendinger,

1992; Burchfiel et al., 1992; DeCelles, 2004; Dickinson, 2004; Evenchick et al., 2007; Yonkee and Weil, 2015). The western portion of the Cordillera consists of a complex patchwork of lithotectonic terranes that were accreted to the western edge of North America during Mesozoic subduction (e.g., Coney et al., 1980; Monger et al., 1982; Dickinson, 2004; Nelson et al., 2013). These terranes, which consist of a series of late Paleozoic to Mesozoic island arcs and accretionary complexes, form a critically important province of the Cordillera, and investigations of their complex histories of collision and margin-parallel translation have illuminated the paleogeography and tectonic dynamics of the eastern Pacific realm (e.g., Jones et al., 1977; Rusmore et al., 1988; Edelman and Sharp, 1989; McClelland et al., 1992; Avé Lallemant, 1995; Wyld and Wright, 2001; Evenchick et al., 2007; Dickinson, 2008; Ernst et al., 2008; LaMaskin et al., 2011; Riddell, 2011).

In west-central Idaho, the Salmon River suture zone demarcates the boundary between rocks of North American affinity on the east and accreted rocks of the Wallowa island arc terrane, which is the northernmost of four mapped terranes of the Blue Mountains Province, on the west (Fig. 1A) (e.g., Hamilton, 1969; Vallier, 1977; Silberling et al., 1984; Lund and Snee, 1988; Selverstone et al., 1992; Schwartz et al., 2010; LaMaskin et al., 2015). Accretion of the Wallowa terrane onto the western North American margin resulted in Cretaceous burial-related metamorphism and diffuse ductile contractional deformation that are observed across the ~30–40-km-wide, north-striking Salmon River suture zone (Fig. 1B) (e.g., Selverstone et al., 1992; Getty et al., 1993; Blake et al., 2009; McKay et al., 2017; Gray et al., 2020). The suture zone deforms accreted metavolcanic and metasedimentary rocks that have been divided into lithotectonic packages separated by east-dipping thrust faults, which transition eastward into a domain dominated by syn-deformational intrusive rocks (e.g., Hamilton, 1969; Selverstone et al., 1992; Manduca et al., 1993; Lund, 2004; Gray, 2013a, 2013b). However, all structural levels of the suture zone exhibit penetrative ductile fabrics, irrespective of their location relative to mapped thrust faults (e.g., Blake, 1991; Gray et al., 2020), which brings into question the dominant processes of mass transfer, the spatial distribution of strain (i.e., distributed versus localized), and the kinematic paths of the lithotectonic packages within the suture zone.

In this study, we investigate these questions by integrating structural analysis of the Salmon River suture zone with a detailed examination of its thermal architecture. We utilize Raman spectroscopy of carbonaceous material (RSCM) thermometry to measure peak metamorphic temperatures from 32 metasedimentary samples collected across the range of structural levels exposed in the suture zone, which we integrate with published thermobarometry (Selverstone et al., 1992; McKay, 2011; Bollen, 2015; McKay et al., 2017) to quantify temperature patterns within thrust sheets and the spatial extent of inverted thermal gradients across mapped thrust faults. We interpret our results in the context of published pressure-temperature-time data (Lund and Snee, 1988; Selverstone et al., 1992; Getty et al., 1993; Snee et al., 1995; McKay et al., 2017) in order to elucidate the structural evolution of the suture zone. As the Salmon River suture zone represents a well-characterized case study of a ductile accretionary complex constructed during arc-continent collision, insights gained in this study can be applied globally to investigate analogous accretionary margins elsewhere.

## 2. TECTONOSTRATIGRAPHIC AND TEMPORAL FRAMEWORK OF THE SALMON RIVER SUTURE ZONE

The Salmon River suture zone is a north-south–striking, ~30–40-km-wide zone of deformation that exhibits pervasive ductile fabrics (Fig. 1B) (e.g., Blake et al., 2009; Gray et al., 2020). The suture zone was constructed within a complex geologic framework that included Neoproterozoic–Paleozoic sedimentary rocks of North American (i.e., Laurentian) affinity on the east and structurally imbricated Permian–Jurassic volcanic and sedimentary rocks of the Wallowa island arc terrane on the west, as well as pre- and syn-deformational intrusive rocks that span a protracted emplacement history (e.g., Hamilton, 1969; Lund and Snee, 1988; Selverstone et al., 1992; Getty et al., 1993; Manduca et al., 1993; Vallier, 1995; Gray and Oldow, 2005; Blake et al., 2009; McKay et al., 2017; Gray et al., 2020). The approximate boundary between Laurentian affinity and accreted rocks is interpreted to lie along the initial $^{87}Sr/^{86}Sr$ ($Sr_I$) ~0.706 isopleth (Fig. 1), which represents the transition between $Sr_I$ values ≤0.704 measured in Permian–Cretaceous calc-alkaline plutons to the west (oceanic crustal affinity) and $Sr_I$ values ≥0.708 measured in Cretaceous calk-alkaline plutons to the east (continental crustal affinity) (Armstrong et al., 1977; Fleck and Criss, 1985, 2004; Manduca et al., 1992; Criss and Fleck, 1987).

Here, we describe the tectonostratigraphic packages of the Salmon River suture zone that have been defined at the latitude of three across-strike transects that we investigated in this study (the Salmon River, Whitebird Ridge, and Pollock Mountain transects; Figs. 1–3). Where applicable, we use the "thrust sheet" terminology common in fold-thrust belts (e.g., Boyer and Elliott, 1982), in which we refer to packages of rock in the Salmon River suture zone by the name of the thrust fault mapped at their base. We also summarize published constraints on the timing of magmatism, metamorphism, and deformation in the suture zone. This discussion is organized from west to east and is supported by tectonostratigraphic columns of each transect (Fig. 4) and a compilation of published geochronology (Table 1; Fig. 5). Readers are referred to Gray and Oldow (2005), Blake et al. (2009), and Gray et al. (2020) for detailed descriptions and interpretations of the ductile fabrics of the Salmon River suture zone at our studied latitude.

### 2.1. Heavens Gate Thrust Sheet and Underlying Wallowa Terrane Rocks

Rocks on the eastern flank of Hells Canyon are dominated by lower greenschist-facies andesite, basalt, volcaniclastic rocks, and sedimentary rocks of the Triassic Wild Sheep Creek Formation, which are interpreted as accreted rocks of the Wallowa terrane (Figs. 1B and 2) (Vallier, 1977, 1995;

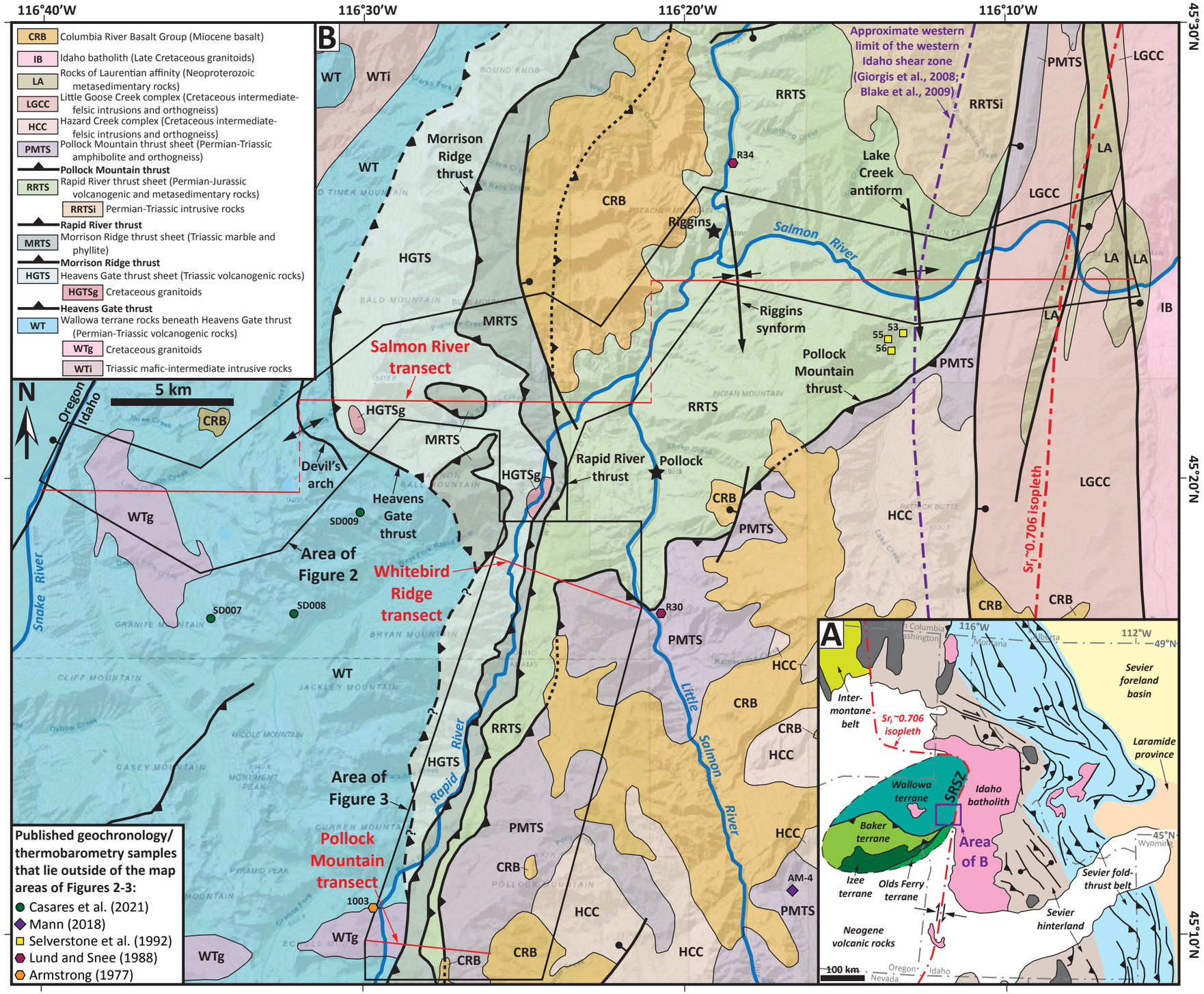


Figure 1. (A) Map of structural and magmatic provinces of the Cordilleran orogen, showing accreted terranes of the Blue Mountains Province (Wallowa, Baker, Izee, and Olds Ferry terranes) (modified from Gray et al., 2020; their fig. 1A). Dark-gray polygons are mid-crustal rocks exhumed within metamorphic core complexes. SRSZ is the Salmon River suture zone. (B) Geologic map of a portion of west-central Idaho showing tectonostratigraphic divisions of the SRSZ and the locations of the Salmon River, Whitebird Ridge, and Pollock Mountain transects. The eastern edge of the map area demarcates the approximate eastern limit of ductile deformation associated with the SRSZ, and the map trace of the Heavens Gate thrust demarcates the approximate western limit (e.g., Gray et al., 2020). Published geochronology and thermobarometry samples discussed in the text that lie outside of the map areas of Figures 2 and 3 are shown. Map is modified from Schmidt et al. (2016; their fig. 4), McKay et al. (2017; their fig. 1), and Gray et al. (2020; their fig. 2).

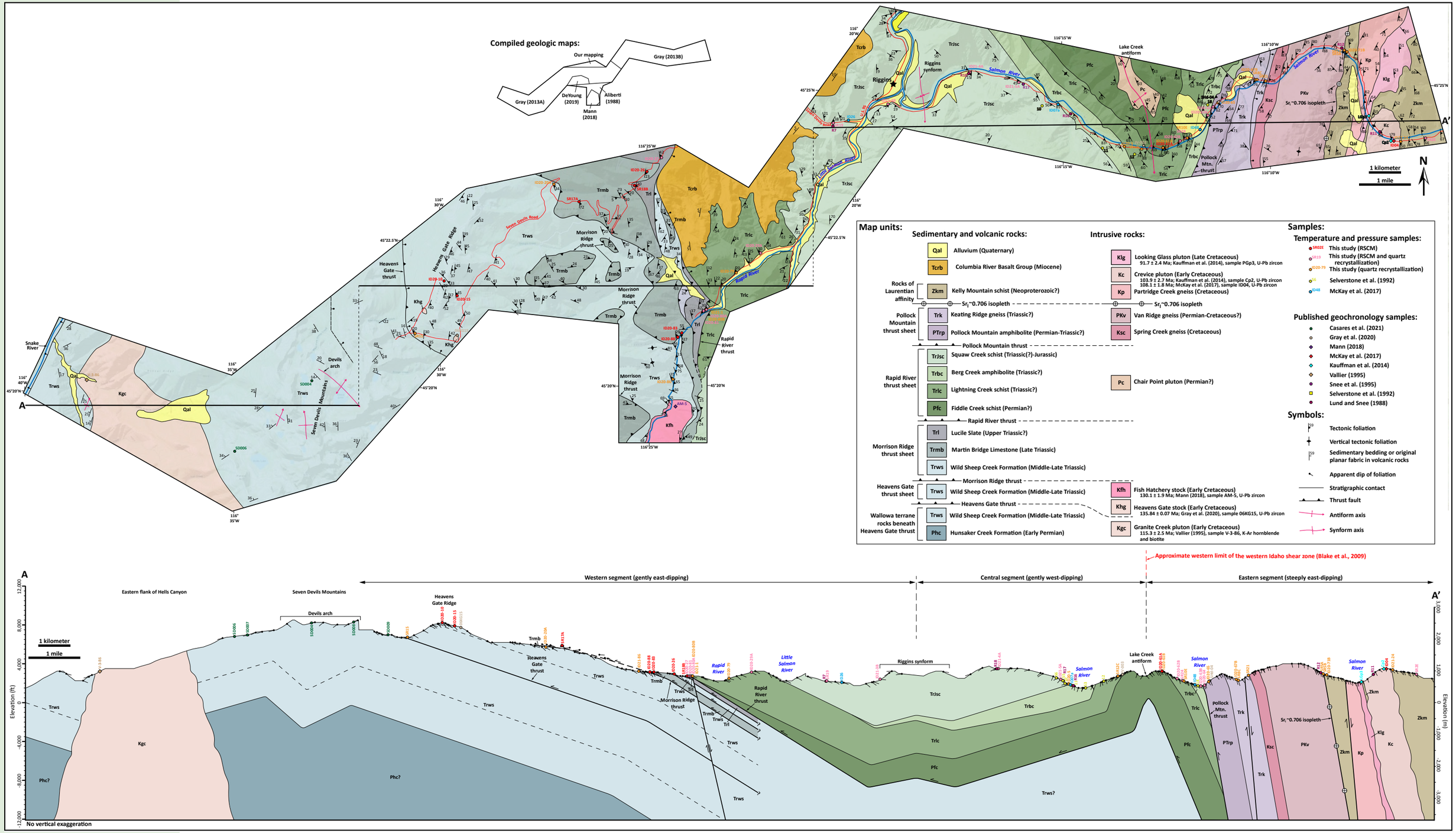


To view Figure 2 at full size, please visit https://doi.org/10.1130/GEOS.S.22764377 or access the full-text article on www.gsapubs.org.

**Figure 2. Geologic map (1:48,000 scale) of the Salmon River transect (top) and accompanying geologic cross section A–A′ (bottom). Geologic map compiled from Aliberti (1988), Gray (2013a, 2013b), Mann (2018), DeYoung (2019), and our mapping. The location of the map area is shown on Figure 1B. Timing constraints for rock units are from Gray (2013a, 2013b) and Gray et al. (2020) unless otherwise specified. The subsurface geometry beneath the Rapid River thrust is queried in the eastern part of the cross section. To view Figure 2 at full size, please visit https://doi.org/10.1130/GEOS.S.22764377 or access the full-text article on www.gsapubs.org.**

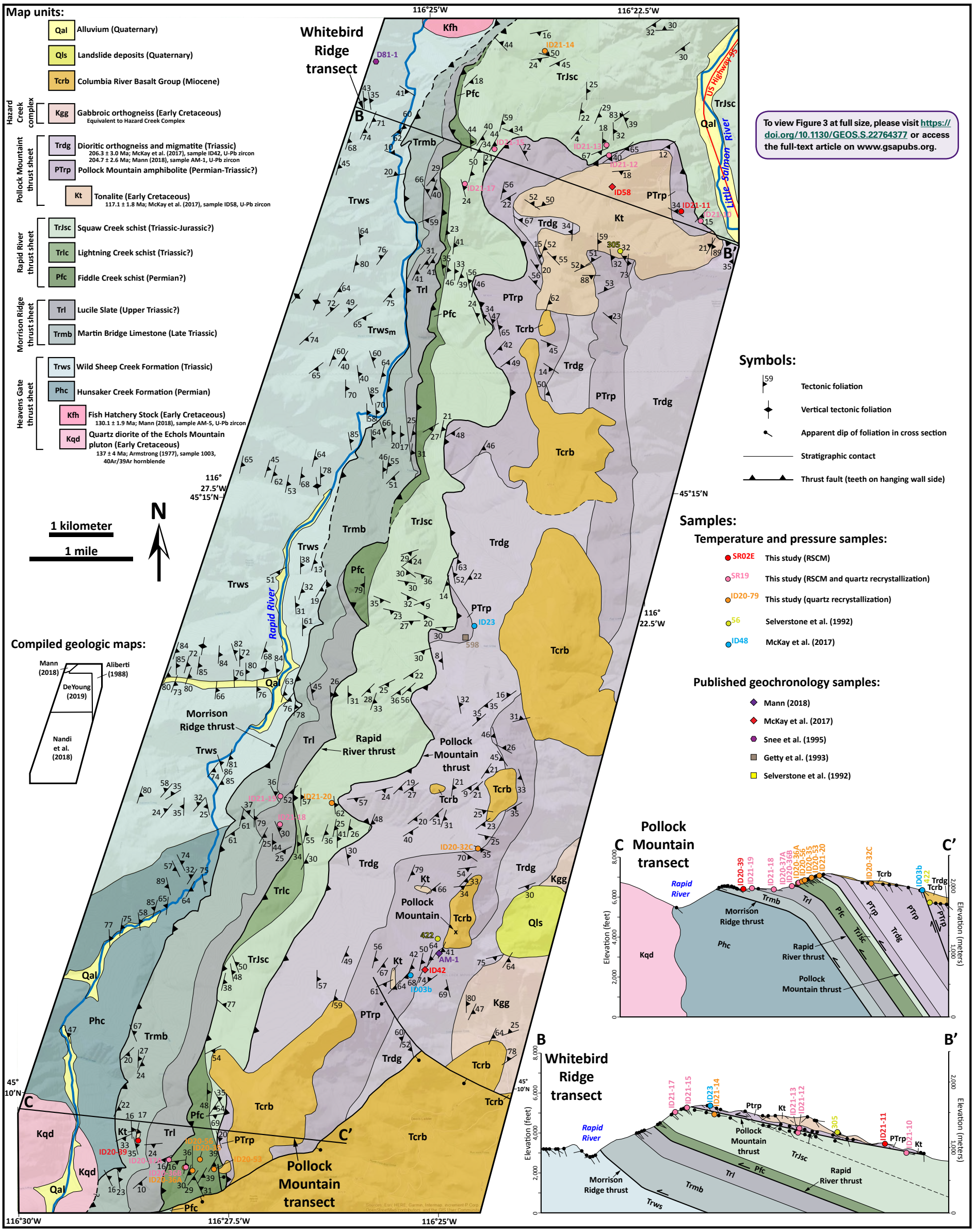


Figure 3. Geologic map (1:48,000 scale) that includes the Whitebird Ridge transect (B–B′ cross-section line) and Pollock Mountain transect (C–C′ cross-section line) and accompanying geologic cross sections. Map is compiled from Aliberti (1988), Mann (2018), Nandi et al. (2018), and DeYoung (2019). The location of the map area is shown on Figure 1B. Timing constraints for rock units are from Gray (2013a, 2013b) and Gray et al. (2020) unless otherwise specified. To view Figure 3 at full size, please visit https://doi.org/10.1130/GEOS.S.22764377 or access the full-text article on www.gsapubs.org.

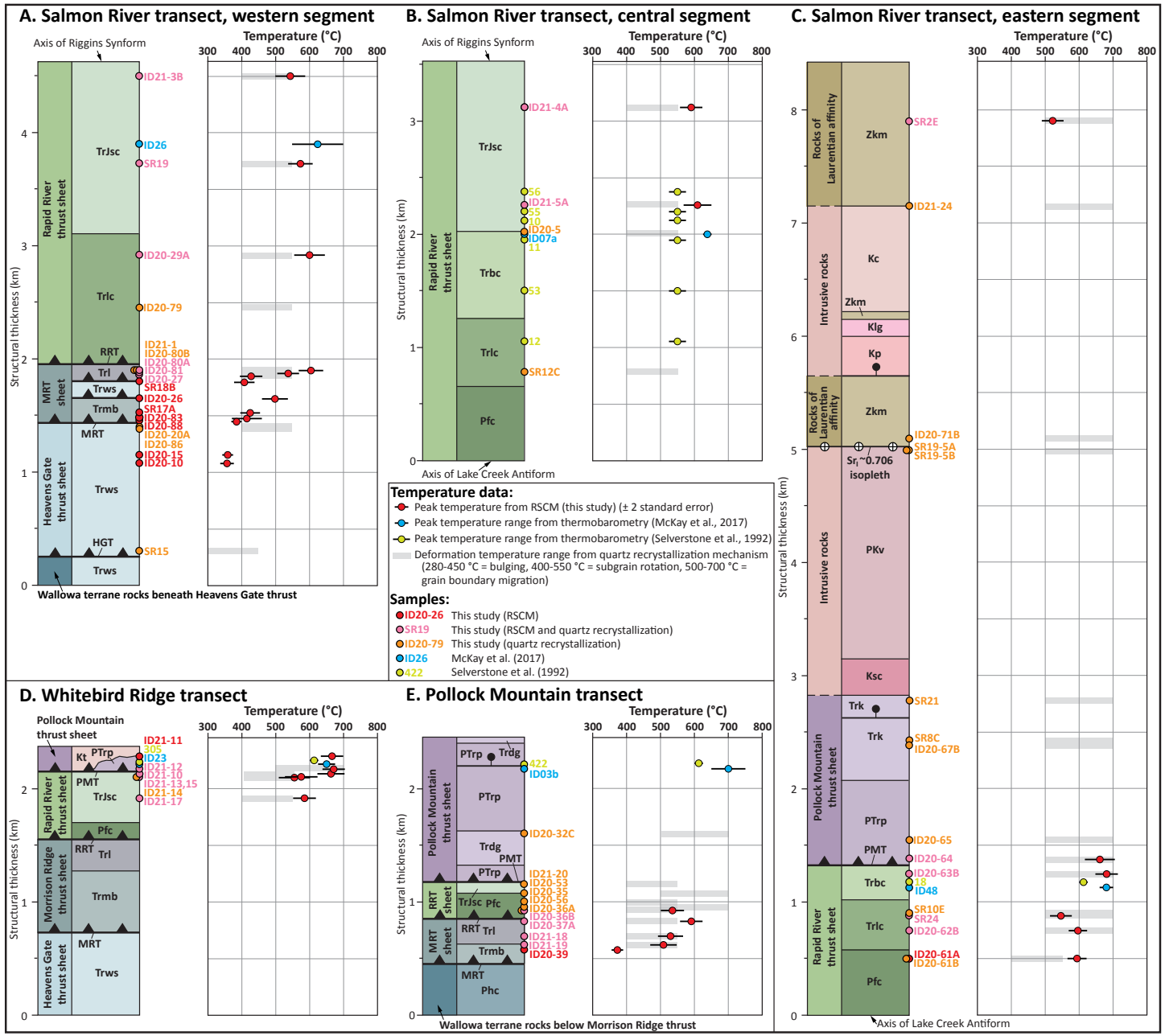


**Figure 4. Tectonostratigraphic columns of the Salmon River (A–C), Whitebird Ridge (D), and Pollock Mountain (E) transects, which plot structural (i.e., foliation-normal) thickness relative to the lowest structural level exposed on the corresponding cross sections on Figures 2 and 3. The positions of Raman spectroscopy of carbonaceous material (RSCM) and quartz recrystallization samples from this study are plotted, as well as the positions of samples from Selverstone et al. (1992) and McKay et al. (2017). Temperature data are graphed versus structural thickness to the right of each column. Abbreviations: HGT—Heavens Gate thrust; MRT—Morrison Ridge thrust; PMT—Pollock Mountain thrust; RRT—Rapid River thrust. See Figures 2 and 3 for a guide to rock unit abbreviations.**

TABLE 1. COMPILATION OF PUBLISHED GEOCHRONOLOGY FROM SALMON RIVER SUTURE ZONE SAMPLES, LISTED FROM WEST TO EAST FOR EACH OF THE INVESTIGATED TRANSECTS

| Dated rock unit | Age (Ma) and error | Technique | Age interpretation | Source publication | Sample | Location relative to section line |
|---|---|---|---|---|---|---|
| Salmon River transect | | | | | | |
| *Wallowa Terrane rocks below Heavens Gate thrust* | | | | | | |
| Granite Creek Pluton | 115.3 ± 2.5 | K-Ar hornblende, biotite | Post-magmatic cooling | Vallier (1995) | V-3-86 | 0.5 km to north |
| Intrusion within unit Trws | 123 ± 2.0 | U-Pb zircon | Magmatic crystallization | Casares et al. (2021) | SD006 | 1.5 km to south |
| Intrusion within unit Trws | 120 ± 1.0 | U-Pb zircon | Magmatic crystallization | Casares et al. (2021) | SD007 | 5 km to south |
| Intrusion within unit Phc | 226 ± 10 | U-Pb zircon | Magmatic crystallization | Kauffman et al. (2014) | I | 15 km to north |
| Intrusion within unit Trws | 137 ± 2.0 | U-Pb zircon | Magmatic crystallization | Casares et al. (2021) | SD004 | 1 km to north |
| Intrusion within unit Trws | 120 ± 1.0 | U-Pb zircon | Magmatic crystallization | Casares et al. (2021) | SD008 | 5 km to south |
| Intrusion within unit Trws | 136 ± 2.0 | U-Pb zircon | Magmatic crystallization | Casares et al. (2021) | SD009 | 4 km to south |
| *Heavens Gate thrust sheet* | | | | | | |
| Heavens Gate stock | 135.84 ± 0.07 | U-Pb zircon | Magmatic crystallization | Gray et al. (2020) | 06KG15 | 1.5 km to south |
| Fish Hatchery stock | 130.1 ± 1.9 | U-Pb zircon | Magmatic crystallization | Mann (2018) | AM-5 | 4 km to south |
| *Rapid River thrust sheet* | | | | | | |
| Squaw Creek schist | 117.0 ± 0.5 | Ar/Ar hornblende | Exhumation-related cooling | Lund and Snee (1988) | R7 | Along section line |
| Squaw Creek schist | 124.3 ± 5.8 | Sm-Nd garnet | Prograde metamorphism | McKay et al. (2017) | ID26 | Along section line |
| Squaw Creek schist | 109.1 ± 0.6 | Ar/Ar hornblende | Exhumation-related cooling | Lund and Snee (1988) | R34 | 4 km to north |
| Squaw Creek schist | 106.5 ± 1.4 | Ar/Ar hornblende | Exhumation-related cooling | Lund and Snee (1988) | R18 | 1.5 km to north |
| Squaw Creek schist | 106.8 ± 0.5 | Ar/Ar hornblende | Exhumation-related cooling | Snee et al. (1995) | R17 | 1.3 km to north |
| Berg Creek amphibolite | 88.2 ± 0.5 | Ar/Ar biotite | Exhumation-related cooling | Lund and Snee (1988) | R16 | 0.5 km to north |
| Fiddle Creek schist | 119.8 ± 6.7 | Lu-Hf garnet | Prograde metamorphism | Gray et al. (2020) | JV-003 | 0.5 km to south |
| Berg Creek amphibolite | 112.5 ± 1.5 | Sm-Nd garnet | Prograde metamorphism | McKay et al. (2017) | ID48 | Along section line |
| *Pollock Mountain thrust sheet* | | | | | | |
| Dike intruding unit PTrp | 90.62 ± 0.23 | U-Pb zircon | Magmatic crystallization | Gray et al. (2020) | SHd-04 | 0.5 km to north |
| Van Ridge gneiss | 82.5 ± 0.4 | Ar/Ar biotite | Post-magmatic cooling | Lund and Snee (1988) | R12 | 2.5 km to north |
| *Intrusive rocks in the eastern part of the Salmon River suture zone* | | | | | | |
| Looking Glass Pluton | 91.7 ± 2.4 | U-Pb zircon | Magmatic crystallization | Kauffman et al. (2014) | LGp3 | Along section line |
| Crevice Pluton | 85.1 ± 0.4 | Ar/Ar hornblende | Post-magmatic cooling | Lund and Snee (1988) | R11 | 0.5 km to south |
| Crevice Pluton | 103.9 ± 2.7 | U-Pb zircon | Magmatic crystallization | Kauffman et al. (2014) | CP2 | 0.5 km to south |
| Crevice Pluton | 108.1 ± 1.8 | U-Pb zircon | Magmatic crystallization | McKay et al. (2017) | ID04 | 0.5 km to south |
| *Idaho Batholith* | | | | | | |
| Western margin of the batholith | 76.7 ± 0.4 | Ar/Ar muscovite | Post-magmatic cooling | Lund and Snee (1988) | R10 | 2.5 km to east |
| Western margin of the batholith | 90.4 ± 0.8 | U-Pb zircon | Magmatic crystallization | McKay et al. (2017) | PRC01 | 5 km to east |
| Western margin of the batholith | 75.3 ± 0.4 | Ar/Ar muscovite | Post-magmatic cooling | Lund and Snee (1988) | R8 | 6 km to east |
| Western margin of the batholith | 74.7 ± 0.4 | Ar/Ar biotite | Post-magmatic cooling | Lund and Snee (1988) | R8 | 6 km to east |
| Western margin of the batholith | Ca. 86–93 | U-Pb zircon | Magmatic crystallization | Gray et al. (2020) | FC-05 | 7.5 km to east |
| Whitebird Ridge transect | | | | | | |
| *Wallowa Terrane rocks below Morrison Ridge thrust* | | | | | | |
| Tonalite intruding unit Twrs | 145.1 ± 1.5 | Ar/Ar hornblende | Post-magmatic cooling | Snee et al. (1995) | D81-1 | 1 km to north |
| *Pollock Mountain thrust sheet* | | | | | | |
| Pollock Mountain amphibolite | 119 ± 2 | Ar/Ar hornblende | Exhumation-related cooling | Getty et al. (1993) | 598 | 7 km to south |
| Pollock Mountain amphibolite | 128 ± 3 | Sm-Nd garnet | Prograde metamorphism | Getty et al. (1993) | 598 | 7 km to south |
| Pollock Mountain amphibolite | 135 ± 2.4 to 123.9 ± 1.3 | Sm-Nd garnet | Prograde metamorphism | McKay et al. (2017) | ID23 | 7 km to south |
| Tonalite intruding unit PTrp | 117.1 ± 1.8 | U-Pb zircon | Magmatic crystallization | McKay et al. (2017) | ID58 | Along section line |
| Pollock Mountain amphibolite | 118.0 ± 0.6 | Ar/Ar hornblende | Exhumation-related cooling | Lund and Snee (1988) | R30 | 1 km to east |
| Pollock Mountain transect | | | | | | |
| *Wallowa Terrane rocks below Morrison Ridge thrust* | | | | | | |
| Echols Mountain pluton | 137 ± 4 | Ar/Ar hornblende | Post-magmatic cooling | Armstrong et al. (1977) | 1003 | 1.5 km to north |
| *Pollock Mountain thrust sheet* | | | | | | |
| Pollock Mountain amphibolite | 136.9 ± 3.5 | Sm-Nd garnet | Prograde metamorphism | McKay et al. (2017) | ID03b | 3 km to north |
| Pollock Mountain amphibolite | >144 (core)–136 (rim) | Sm-Nd garnet | Prograde metamorphism | Getty et al. (1993) | 422 | 3.5 km to north |
| Orthogneiss (unit Trdg) | 140.5 ± 3.9 (rims) | U-Pb zircon | Prograde metamorphism | McKay et al. (2017) | ID42 | 3 km to north |
| Orthogneiss (unit Trdg) | 206.3 ± 3.0 (cores) | U-Pb zircon | Magmatic crystallization | McKay et al. (2017) | ID42 | 3 km to north |
| Orthogneiss (unit Trdg) | 204.7 ± 2.6 | U-Pb zircon | Magmatic crystallization | Mann (2018) | AM-1 | 3.5 km to north |
| *Intrusive rocks in the eastern part of the Salmon River suture zone* | | | | | | |
| Hazard Creek complex | 113.7 ± 1.6 | U-Pb zircon | Magmatic crystallization | Mann (2018) | AM-2 | 12 km to east and 4 km to south |
| Hazard Creek complex | 107.7 ± 2.9 | U-Pb zircon | Magmatic crystallization | Mann (2018) | AM-3 | 12 km to east and 4 km to south |
| Hazard Creek complex | 114.4 ± 2.2 | U-Pb zircon | Magmatic crystallization | Unruh et al. (2008) | K92-8 | 12 km to east and 2.5 km to south |
| Hazard Creek complex | 112.2 ± 1.6 | U-Pb zircon | Magmatic crystallization | Mann (2018) | AM-4 | 12.5 km to east and 2.5 km to north |
| Hazard Creek complex | 118 ± 5 | U-Pb zircon | Magmatic crystallization | Manduca et al. (1993) | 83z9 | 19 km to east and 5 km to south |
| Little Goose Creek complex | 110 ± 5 | U-Pb zircon | Magmatic crystallization | Manduca et al. (1993) | 83z14 | 23 km to east and 4 km to north |
| Little Goose Creek complex | 105.2 ± 1.5 | U-Pb zircon | Magmatic crystallization | Giorgis et al. (2008) | 99mg | 24 km to east and 4 km to north |
| *Idaho Batholith* | | | | | | |
| Western margin of the batholith | 91.5 ± 1.1 | U-Pb zircon | Magmatic crystallization | Giorgis et al. (2008) | 01-53 | 26 km to east and 2 km to south |

*Notes:* Sample locations are shown on Figures 1–3 (with the exception of Idaho batholith samples from the Salmon River and Pollock Mountain transects and samples from the Hazard Creek and Little Goose Creek complexes from the Pollock Mountain transect, which lie to the east and southeast of the area shown on Figure 1B).

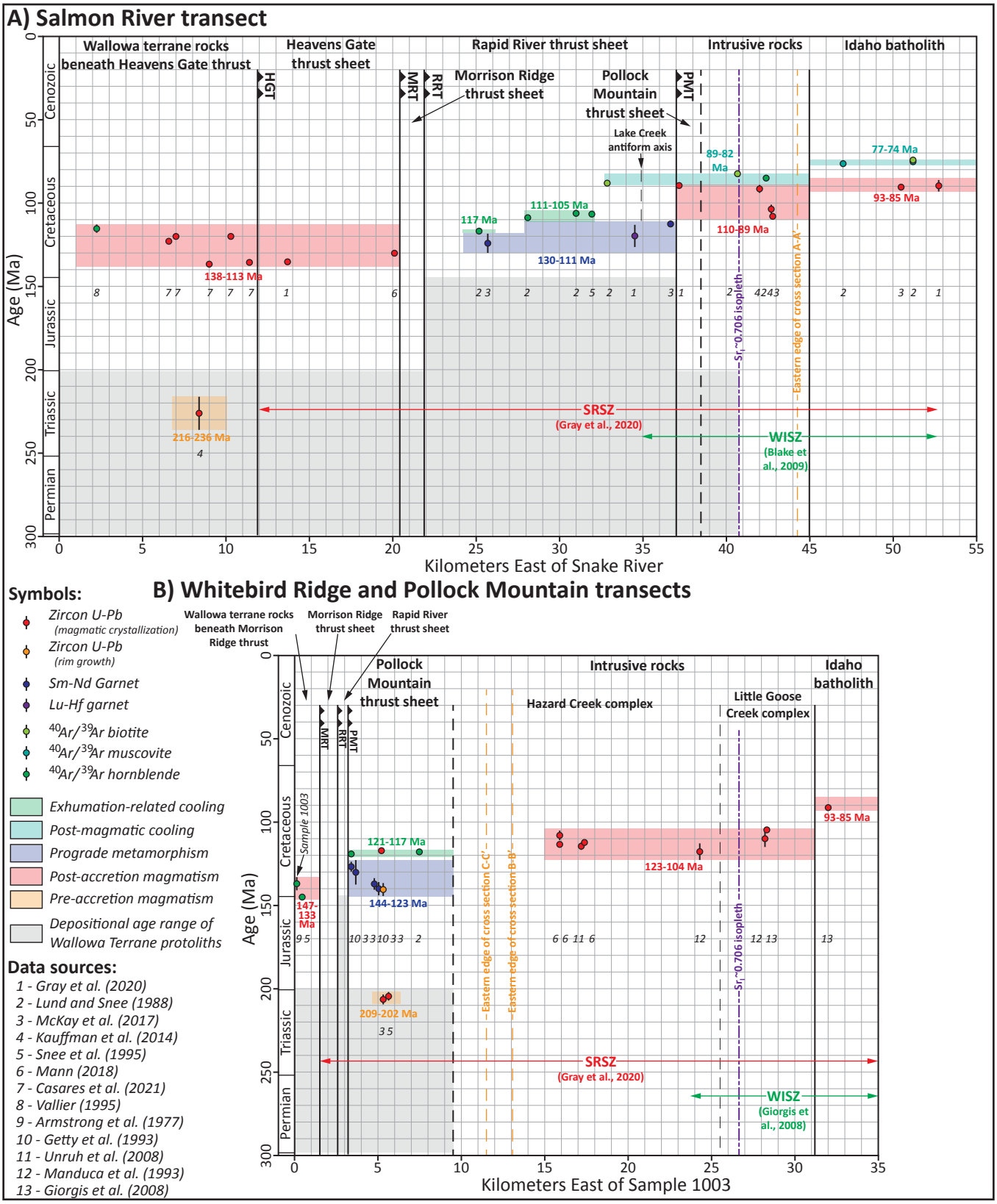


**Figure 5. Compilation of published geochronology from samples collected along and proximal to (A) the Salmon River transect and (B) the Whitebird Ridge and Pollock Mountain transects, presented as graphs of age versus west-to-east distance. Tectonostratigraphic divisions are labeled, as well as age ranges for magmatism, prograde metamorphism, and cooling. Small numbers in italics are referenced to data source publications. See Table 1 for additional details on samples and ages. Abbreviations: HGT—Heavens Gate thrust; MRT—Morrison Ridge thrust; PMT—Pollock Mountain thrust; RRT—Rapid River thrust; SRSZ—Salmon River suture zone; WISZ—western Idaho shear zone.**

Lund, 1984; Gray and Oldow, 2005; Gray, 2013a; Schmidt et al., 2016). Along the Salmon River transect, a 1.2-km-thick (note: all thicknesses listed in this study are foliation-normal structural thicknesses) sheet of the Wild Sheep Creek Formation that exhibits penetrative ductile fabrics is exposed above the east-dipping Heavens Gate thrust (Figs. 2 and 4A) (Gray and Oldow, 2005; Gray, 2013a). The Heavens Gate thrust places penetratively deformed rocks in its hanging wall over rocks that preserve original depositional textures in its footwall (Gray and Oldow, 2005), which led Gray et al. (2020) to interpret this fault as the basal structural level of deformation associated with the Salmon River suture zone. Gray et al. (2020) interpreted a top-to-the-west displacement sense for the Heavens Gate thrust at the latitude of the Salmon River transect based on west-vergent sigmoidal strain markers and asymmetrically sheared conglomerate clasts observed in its hanging wall. The southward continuation of the Heavens Gate thrust is uncertain at the latitude of the Whitebird Ridge and Pollock Mountain transects (Fig. 1B). Gray et al. (2020) showed the queried trace of the Heavens Gate thrust merging with the Morrison Ridge thrust ~2 km to the north of the Pollock Mountain transect.

Along the Salmon River transect, a 135.84 ± 0.07 Ma diorite body (U-Pb zircon; Gray, 2013a; Gray et al., 2020) intrudes rocks in the hanging wall of the Heavens Gate thrust (Fig. 2). The diorite body exhibits ductile fabrics that have been attributed to shearing on the Heavens Gate thrust, which constrains thrust displacement as ca. 136 Ma or younger (Gray et al., 2020).

### 2.2. Morrison Ridge Thrust Sheet

On the Salmon River transect, a 0.5 km cumulative thickness of penetratively deformed Triassic clastic (Lucile Slate), carbonate (Martin Bridge Limestone), and volcanic (Wild Sheep Creek Formation) rocks are imbricated within a system of closely spaced thrust faults above the Heavens Gate thrust sheet (Onasch, 1977, 1987; Sarewitz, 1982; Aliberti, 1988; Gray, 2013a) (Figs. 2 and 4A). The basal fault of this system is the Morrison Ridge thrust (Gray and Oldow, 2005), which places the Martin Bridge Limestone over volcanic rocks of the Wild Sheep Creek Formation. Gray and Oldow (2005) interpreted a top-to-the-west displacement sense for the Morrison Ridge thrust, on the basis of west-vergent isoclinal folds observed in its footwall and hanging wall. On the Salmon River transect, two unnamed thrust faults are mapped between the Morrison Ridge thrust and the overlying Rapid River thrust (Fig. 2) (Gray, 2013a). For simplicity, we refer to the entire structurally imbricated package of rocks carried between the Morrison Ridge and Rapid River thrusts as the Morrison Ridge thrust sheet on the Salmon River transect (Figs. 2 and 4A). On the Whitebird Ridge and Pollock Mountain transects, the Morrison Ridge thrust carries a sheet of the Martin Bridge Limestone and Lucile Slate that is 0.8 km thick and 0.4 km thick, respectively (Nandi et al., 2018; DeYoung, 2019) (Figs. 3, 4D, and 4E).

Four km to the south of the Salmon River transect, tonalite of the 130.1 ± 1.9 Ma Fish Hatchery Stock (U-Pb zircon; Gray and Isakson, 2016; Mann, 2018) intrudes rocks in the footwall of the Morrison Ridge thrust (Fig. 2). The structurally highest part of the stock exhibits penetrative ductile fabrics that have been attributed to shearing on the Morrison Ridge thrust (Gray and Isakson, 2016; Mann, 2018), which constrains thrust displacement as ca. 130 Ma or younger (Gray et al., 2020).

### 2.3. Rapid River Thrust Sheet

The east-dipping Rapid River thrust (Figs. 1–3) (e.g., Hamilton, 1963, 1969; Onasch, 1987; Aliberti, 1988) structurally bounds the top of the Morrison Ridge thrust sheet. The Rapid River thrust was originally mapped by Hamilton (1963, 1969) at an upward transition in lithology and metamorphic grade defined by amphibolite-facies (garnet-, oligoclase-, and andesine-bearing) metavolcanic and metasedimentary rocks overlying greenschist-facies marble and phyllite. Hamilton (1969) documented that the Rapid River thrust locally truncates the garnet-in isograd and interpreted it as a top-to-the-west, syn- to post-metamorphic structure. The Rapid River thrust carries penetratively deformed metavolcanic and metasedimentary rocks that are interpreted to be derived from Permian–Jurassic protoliths of the Wallowa terrane (e.g., Hamilton, 1963). On the Salmon River transect, the Rapid River thrust sheet is at least 3.5 km thick (Figs. 2 and 4A–4C) and is composed of (in ascending order) the Fiddle Creek schist (garnet-muscovite-biotite schist), Lightning Creek schist (chlorite-muscovite schist, garnet-biotite-hornblende schist, and meta-volcanic agglomerate), Berg Creek amphibolite (garnet amphibolite), and Squaw Creek schist (hornblende-biotite schist with local amphibolite) (Blake, 1991; Gray, 2013b). The Rapid River thrust sheet is folded across the open Riggins synform and the tight Lake Creek antiform (Gray, 2013b) (Figs. 1B and 2), which divide the Salmon River transect into a gently east-dipping western segment, a gently west-dipping central segment, and a steeply east-dipping eastern segment (Figs. 2 and 4A–4C). The thickness of the Rapid River thrust sheet decreases southward to 0.6 km on the Whitebird Ridge transect and 0.3 km on the Pollock Mountain transect (Figs. 1, 3, 4D, and 4E). Along these two transects, only the Fiddle Creek schist and overlying Squaw Creek schist are exposed (Nandi et al., 2018; DeYoung, 2019).

Along the Salmon River transect, prograde metamorphism of rocks in the Rapid River thrust sheet is recorded by Sm-Nd and Lu-Hf garnet growth ages between ca. 130–111 Ma (Fig. 5A) (McKay et al., 2017; Gray et al., 2020), which McKay et al. (2017) interpreted as the timing of structural burial. The Rapid River thrust sheet cooled through ~500 °C ($^{40}Ar/^{39}Ar$ hornblende; e.g., Dahl, 1996) at ca. 117 Ma in the western part of the sheet and at ca. 111–105 Ma in the central part of the sheet (Fig. 5A) (Lund and Snee, 1988; Snee et al., 1995). McKay et al. (2017) interpreted that these ages represent the timing of exhumation-related cooling initiated by top-to-the-west displacement on the Rapid River thrust. Their interpretation is supported by Selverstone et al. (1992), who utilized thermobarometry and the $^{40}Ar/^{39}Ar$ hornblende ages of Lund and Snee (1988) to constrain the P-T-t path of rocks in the central part of the Rapid

River thrust sheet. Selverstone et al. (1992) documented exhumation from peak metamorphic conditions of ~8 kbar and ~550 °C to an episode of retrograde metamorphism along the exhumation path at ~6 ± 1 kbar and ~475–500 °C at ca. 111–105 Ma. This indicates that rocks in the Rapid River thrust sheet had experienced ~3.7–11.1 km of exhumation (assuming a lithostatic gradient of 3.7 km/kbar) by the time they cooled through ~500 °C at ca. 111–105 Ma, and thus that top-to-the-west displacement on the Rapid River thrust had initiated by this time (Selverstone et al., 1992).

### 2.4. Pollock Mountain Thrust Sheet

The Pollock Mountain thrust (Figs. 1–3) (e.g., Hamilton, 1969; Aliberti, 1988; Blake, 1991; Selverstone et al., 1992) structurally bounds the top of the Rapid River thrust sheet. The Pollock Mountain thrust was originally mapped by Hamilton (1963, 1969) as an east-dipping thrust fault in some places and in other places as a gradational contact between metavolcanic rocks and an overlying package of interlayered amphibolite and intrusive rocks on the east. Following this, Selverstone et al. (1992) interpreted the Pollock Mountain thrust as a syn- to late-metamorphic thrust fault or thrust-sense shear zone that placed hanging wall rocks that experienced peak metamorphic conditions of ~9–11 kbar and ~600–625 °C over footwall rocks that experienced ~8 kbar and ~550 °C. Shear-sense indicators that are spatially distributed in the hanging wall and footwall of the Pollock Mountain thrust are consistent with a top-to-the-west displacement sense (e.g., Blake, 1991; Blake et al., 2009; McKay et al., 2017; Gray et al., 2020). The hanging wall of the Pollock Mountain thrust sheet is dominated by upper amphibolite-facies metaigneous rocks with local metasedimentary intervals, which are interpreted to be derived from Permian–Triassic protoliths of accreted island arc rocks (e.g., Aliberti, 1988; Blake, 1991; Selverstone et al., 1992). The eastern extent of the Pollock Mountain thrust sheet can only be approximated by the easternmost exposures of Permian–Triassic rocks, as Cretaceous intrusive rocks become volumetrically dominant moving eastward (Fig. 1B).

On the Salmon River transect, the Pollock Mountain thrust sheet consists of a 1.5-km-thick package of garnet amphibolite, biotite-hornblende gneiss, and garnet-biotite schist (Blake, 1991; Gray, 2013b) (Fig. 4C). On the Whitebird Ridge transect, the thrust sheet consists of at least 0.2 km of garnet amphibolite, which is intruded by ca. 117 Ma tonalite (U-Pb zircon; McKay et al., 2017; DeYoung, 2019) (Fig. 4D). On the Pollock Mountain transect, the thrust sheet consists of at least 1.3 km of interlayered garnet amphibolite and dioritic orthogneiss, which locally preserve migmatitic textures (McKay et al., 2017; Nandi et al., 2018) (Fig. 4E).

Along the Pollock Mountain and Whitebird Ridge transects, prograde metamorphism of rocks in the Pollock Mountain thrust sheet is recorded by Sm-Nd garnet growth ages between ca. 144–123 Ma (Getty et al., 1993; McKay et al., 2017) and U-Pb zircon metamorphic rim growth between ca. 144–137 Ma (McKay et al., 2017) (Fig. 5B). Getty et al. (1993) and McKay et al. (2017) interpreted that these ages record the timing of structural burial of rocks of the Wallowa terrane during the early stages of its accretion with the North American margin. On the Whitebird Ridge transect, rocks in the Pollock Mountain thrust sheet cooled through ~500 °C ($^{40}Ar/^{39}Ar$ hornblende) between ca. 121–117 Ma (Fig. 5B) (Lund and Snee, 1988; Getty et al., 1993; Snee et al., 1995), which McKay et al. (2017) interpreted to record the timing of exhumation-related cooling initiated by top-to-the-west displacement on the underlying Pollock Mountain thrust. Their interpretation is supported by syn-emplacement shearing of a 117.1 ± 1.8 Ma (U-Pb zircon) tonalite that intrudes along the Pollock Mountain thrust on the Whitebird Ridge transect (McKay et al., 2017). The ca. 121–117 Ma exhumation age range of the Pollock Mountain thrust sheet overlaps with the ca. 130–111 Ma timing range of burial of the underlying Rapid River thrust sheet, which led McKay et al. (2017) to interpret that top-to-the-west emplacement of the Pollock Mountain thrust sheet contributed to the burial of the Rapid River thrust sheet.

### 2.5. Cretaceous Intrusive Rocks in the Eastern Part of the Suture Zone, Rocks of Laurentian Affinity, and the Late Cretaceous Idaho Batholith

On the eastern side of the Salmon River suture zone, exposures are dominated by variably deformed, intermediate to felsic, Cretaceous intrusions and orthogneiss, which are interlayered with Permian–Triassic metavolcanic rocks of the Pollock Mountain thrust sheet to the west of the $Sr_I$ ~0.706 isopleth and metasedimentary rocks of interpreted Laurentian affinity to the east of the isopleth (Figs. 1B, 2, and 4C) (e.g., Lund, 2004; Gray, 2013b; Blake et al., 2016). Laurentian-affinity rocks are preserved as interlayers of garnet- and sillimanite-bearing schist, paragneiss and quartzite, which are interpreted to represent metamorphosed Neoproterozoic–Paleozoic sedimentary rocks of the Laurentian passive margin basin (e.g., Lund, 1984; Blake, 1991; Kauffman et al., 2014). On the Salmon River transect (Fig. 2), Laurentian-affinity rocks are represented by the Kelly Mountain schist, which is interpreted to correlate with the Neoproterozoic Windermere Supergroup (Blake, 1991).

Intrusive rocks on the eastern side of the Salmon River transect include tonalitic orthogneiss of likely Cretaceous age to the west of the $Sr_I$ ~0.706 isopleth (Gray et al., 2020) and ca. 104–108 Ma and ca. 92 Ma deformed granitic plutons to the east of the isopleth (Gray, 2013b; Kauffman et al., 2014; McKay et al., 2017) (Fig. 2). To the east of the Whitebird Ridge and Pollock Mountain transects, intrusive rocks include the Hazard Creek Complex on the west and the Little Goose Creek Complex, which straddles the $Sr_I$ ~0.706 isopleth, on the east (Fig. 1B). U-Pb zircon crystallization ages from the Little Goose Creek and Hazard Creek complexes at the latitude of the Pollock Mountain transect range between ca. 123–104 Ma (Fig. 5B) (Manduca et al., 1993; Giorgis et al., 2008; Unruh et al., 2008; McKay et al., 2017; Mann, 2018).

Late Cretaceous granitoids of the Idaho batholith lie to the east of our studied transects (Fig. 1B). U-Pb zircon crystallization ages from samples from the westernmost part of the batholith range between ca. 93–85 Ma (Fig. 5)

(Giorgis et al., 2008; Gaschnig et al., 2010; McKay et al., 2017; Gray et al., 2020). Granitoids of the Idaho batholith are interlayered with Laurentian-affinity metasedimentary rocks on the Salmon River transect (Fig. 1B).

### 2.6. The Western Idaho Shear Zone

Cretaceous intrusive rocks in the eastern part of the Salmon River suture zone, along with the Laurentian-affinity rocks and accreted rocks of the Pollock Mountain thrust sheet into which they intruded, have been deformed into metamorphic tectonites with steeply east-dipping, linear-planar ductile fabrics (Figs. 1B and 2) (Manduca et al., 1993; Giorgis et al., 2008; Blake et al. 2009; Gray, 2013b; Gray et al., 2020). These fabrics are attributed to Late Cretaceous dextral-transpressional shearing within the western Idaho shear zone, which is a north-striking, high-strain zone that accommodated significant east-west shortening (perhaps as much as ~100 km) and northward translation of accreted rocks to its west (e.g., McClelland et al., 2000; Tikoff et al., 2001; Giorgis et al., 2005, 2008).

Our Whitebird Ridge and Pollock Mountain transects are located ~12–18 km to the west of the western Idaho shear zone, which lies within the Little Goose Creek and Hazard Creek complexes at this latitude (Fig. 1B) (Manduca et al., 1993; Giorgis et al., 2008). However, Blake et al. (2009) interpreted that the steeply east-dipping ductile fabrics in the eastern portion of the Salmon River transect, which are observed in all rocks to the east of the Lake Creek antiform axis (Figs. 1B and 2), were generated during Late Cretaceous deformation in the western Idaho shear zone. Under this interpretation, the Pollock Mountain thrust sheet and the easternmost portion of the Rapid River thrust sheet on the Salmon River transect were overprinted by Late Cretaceous dextral-transpressional shearing in the western Idaho shear zone (Blake et al., 2009).

There are differing interpretations between previous studies regarding the timing of shearing in the western Idaho shear zone. Gray et al. (2020) interpreted that the steeply east-dipping fabrics in the eastern part of the Salmon River transect were progressively developed by ductile shearing between ca. 115–86 Ma, and therefore overlapped temporally with the late stages of prograde metamorphism and west-directed emplacement of thrust sheets of the Salmon River suture zone to the west. Under this interpretation, the dextral-transpressional shearing on the western Idaho shear zone is the youngest component of an accretion-related progressive deformation event in the Salmon River suture zone that spanned from ca. 144 Ma until at least ca. 86 Ma. Deformation progressed from an early phase (ca. 144–105 Ma) of margin-normal shortening within the western portion of the suture zone and was followed by a later phase (ca. 115–86 Ma) dominated by dextral-transpressional shearing that overprinted the eastern portion.

Alternatively, dextral-transpressional shearing in the western Idaho shear zone has been interpreted as a younger, temporally distinct event that post-dated the metamorphism and deformation associated with the collision and suturing of island arc terranes to the west (McClelland et al., 2000). Giorgis et al. (2008) bracketed shearing in the western Idaho shear zone between ca. 105–90 Ma in a region 15–45 km along-strike to the south of the Salmon River transect. Montz and Kruckenberg (2017) and Braudy et al. (2017), in a region 120–160 km along-strike to the south, bracketed shearing in the western Idaho shear zone between ca. 104–90 Ma and ca. 101–88 Ma, respectively.

## 3. METAMORPHIC CONDITIONS IN THE SALMON RIVER SUTURE ZONE

### 3.1. Summary of Published Thermobarometry

Metamorphic temperatures and pressures attained by rocks in the Rapid River and Pollock Mountain thrust sheets have been determined by Selverstone et al. (1992) and McKay et al. (2017) (data are summarized on Table 2; sample locations are shown on Figs. 1–3, and temperatures are plotted on Fig. 4). Selverstone et al. (1992) utilized the garnet-biotite thermometer and the garnet-biotite-plagioclase-muscovite, quartz-garnet-kyanite-plagioclase, and aluminum-in-hornblende barometers. McKay et al. (2017) utilized pseudo-section modeling and the Thermo-Calc program of Powell and Holland (1994).

Multiple pressure-temperature determinations from the Rapid River thrust sheet were collected on the Salmon River transect. In the western part of the thrust sheet, models from McKay et al. (2017) predict initial conditions of ~520 °C and ~6 kbar and peak conditions of 600–675 °C and 7.0–8.5 kbar for sample ID26. In the central part of the thrust sheet, models from McKay et al. (2017) predict initial conditions of ~600 °C and 6.3–6.8 kbar and peak conditions of 625–650 °C and ~8.8 kbar for sample ID07a. Selverstone et al. (1992) estimated peak conditions of ~550 °C and ~8 kbar from samples from the central part of the thrust sheet (samples 10, 11, 12, 53, 55, and 56) and final equilibration of these samples at ~475–500 °C and ~5–7 kbar, which they interpreted to record the conditions of an episode of retrograde metamorphism along the exhumation path. In the eastern part of the Rapid River thrust sheet, models from McKay et al. (2017) predict initial conditions of 580–640 °C and 6.0–8.3 kbar and peak conditions of 660–700 °C and 9.5–10 kbar for sample ID48, and Selverstone et al. (1992) estimated peak conditions of 600–625 °C and 8–11 kbar for sample 18. These samples were collected at 200 m and 150 m structural distance below the mapped position of the Pollock Mountain thrust, respectively.

Pressure-temperature determinations from the Pollock Mountain thrust sheet have been collected along and proximal to the Whitebird Ridge and Pollock Mountain transects. On the Whitebird Ridge transect, Selverstone et al. (1992) estimated peak conditions of 600–625 °C and 9–11 kbar from sample 305. Seven km to the south of the Whitebird Ridge transect, models of McKay et al. (2017) predict initial conditions of 550–600 °C and 5.3–5.8 kbar and peak conditions of 625–675 °C and 6.5–9.3 kbar for sample ID23. On the Pollock Mountain transect, models of McKay et al. (2017) predict initial conditions of 650–700 °C and 5.5–7.0 kbar and peak conditions of 650–750 °C and 7.5–8.5 kbar

TABLE 2. COMPILATION OF PUBLISHED THERMOBAROMETRY FROM SALMON RIVER SUTURE ZONE SAMPLES

| Source publication | Sample | Transect | Thrust sheet | Unit | Lithology | Structural height (m) | Technique | $T_{initial}$ (°C) | $P_{initial}$ (kbar) | $T_{peak}$ (°C) | $P_{peak}$ (kbar) | $T_{post\text{-}peak}$ (°C) | $P_{post\text{-}peak}$ (kbar) | Peak depth range (km)[1] |
|---|---|---|---|---|---|---|---|---|---|---|---|---|---|---|
| McKay et al. (2017) | ID26 | Salmon River, western segment | Rapid River thrust sheet | TrJsc | Schist | 3900 | Thermo-Calc | ~520 | ~6 | 600–675 | 7.0–8.5 | — | — | 28.7 ± 2.8 |
| Selverstone et al. (1992) | 56 | Salmon River, central segment | Rapid River thrust sheet | TrJsc | Schist | 2375 | Thermobarometry | — | — | ~550 | ~8 | ~475–500 | ~5–7 | 29.6 ± 1.9* |
| Selverstone et al. (1992) | 55 | Salmon River, central segment | Rapid River thrust sheet | TrJsc | Schist | 2200 | Thermobarometry | — | — | ~550 | — | ~475–500 | ~5–7 | — |
| Selverstone et al. (1992) | 10 | Salmon River, central segment | Rapid River thrust sheet | TrJsc | Schist | 2125 | Thermobarometry | — | — | ~550 | — | ~475–500 | ~5–7 | — |
| McKay et al. (2017) | ID07a | Salmon River, central segment | Rapid River thrust sheet | Trbc | Amphibolite | 2000 | Thermo-Calc | ~600 | 6.3–6.8 | 625-650 | ~8.8 | — | — | 32.6 ± 1.9* |
| Selverstone et al. (1992) | 11 | Salmon River, central segment | Rapid River thrust sheet | Trbc | Amphibolite | 1950 | Thermobarometry | — | — | ~550 | — | ~475–500 | ~5–7 | — |
| Selverstone et al. (1992) | 53 | Salmon River, central segment | Rapid River thrust sheet | Trbc | Amphibolite | 1500 | Thermobarometry | — | — | ~550 | ~8 | ~475–500 | ~5–7 | 29.6 ± 1.9* |
| Selverstone et al. (1992) | 12 | Salmon River, central segment | Rapid River thrust sheet | Trlc | Amphibolite | 1050 | Thermobarometry | — | — | ~550 | ~8 | ~475–500 | ~5–7 | 29.6 ± 1.9* |
| Selverstone et al. (1992) | 18 | Salmon River, eastern segment | Rapid River thrust sheet** | Trbc | Amphibolite | 1175 | Thermobarometry | — | — | 600–625 | 8–11 | — | — | 35.2 ± 5.6 |
| McKay et al. (2017) | ID48 | Salmon River, eastern segment | Rapid River thrust sheet** | Trbc | schist | 1125 | Thermo-Calc | 580–640 | 6.0–8.3 | 660–700 | 9.5–10 | — | — | 36.1 ± 0.9 |
| Selverstone et al. (1992) | 305 | Whitebird Ridge | Pollock Mountain thrust sheet | Kt | Tonalite | 2250 | Thermobarometry | — | — | 600–625 | 9–11 | — | — | 37.0 ± 3.7 |
| McKay et al. (2017) | ID23 | Whitebird Ridge | Pollock Mountain thrust sheet | PTrp | Schist | 2225 | Thermo-Calc | 550–600 | 5.3–5.8 | 625–675 | 6.5–9.3 | — | — | 29.2 ± 5.2 |
| Selverstone et al. (1992) | 422 | Pollock Mountain | Pollock Mountain thrust sheet | PTrp | Amphibolite | 2225 | Thermobarometry | — | — | 600–625 | — | — | — | - |
| McKay et al. (2017) | ID03b | Pollock Mountain | Pollock Mountain thrust sheet | PTrp | Amphibolite | 2175 | Thermo-Calc | 650–700 | 5.5–7.0 | 650–750 | 7.5–8.5 | — | — | 29.6 ± 1.9 |

[1]Calculated assuming a lithostatic pressure gradient of 3.7 km/kbar.

$T_{initial}$ and $P_{initial}$ correspond to the initial, first, or earliest assemblage along the burial path (McKay et al., 2017). $T_{peak}$ and $P_{peak}$ correspond to the peak assemblage. $T_{post\text{-}peak}$ and $P_{post\text{-}peak}$ correspond to the "final equilibration" assemblage for samples of the Rapid River thrust sheet (Selverstone et al., 1992).

*The error range for peak depth for these four samples was calculated assuming an approximate $P_{peak}$ error value of ±0.5 kbar.

**These two samples lie within the interval of inverted temperatures that we interpret to delineate the boundaries of the Pollock Mountain shear zone (Fig. 8A); see text for discussion.

*Notes:* Sample locations are shown on Figures 1–3. See Figures 2 and 3 for a guide to unit abbreviations. Em dashes indicate no data.

for sample ID03b, and Selverstone et al. (1992) estimated a peak temperature of 600–625 °C for sample 422.

### 3.2. Raman Spectroscopy of Carbonaceous Material Thermometry

The degree of structural organization of graphite bonds within carbonaceous material, which originates from the metamorphism of organic matter in sedimentary rocks (e.g., Buseck and Huang, 1985), can be used to quantify peak metamorphic temperature using the RSCM thermometer (e.g., Beyssac et al., 2002, 2003; Rahl et al., 2005; Kouketsu et al., 2014; Lünsdorf et al., 2017). We utilized the RSCM calibrations of Rahl et al. (2005) and Kouketsu et al. (2014) to measure peak metamorphic temperatures attained by 32 metasedimentary rock samples from the Salmon River suture zone. Measurements were performed at the Eyring Materials Center at Arizona State University (supporting data and details on analytical methods are available in the Supplemental Material[1]).

Examples of representative Raman spectra and photomicrographs of analyzed grains of carbonaceous material are shown in Figure 6. We followed the procedures of Rahl et al. (2005) and Kouketsu et al. (2014), which involved fitting as many as five Raman peaks (G, D1, D2, D3, and D4) in the wavenumber range of 1000–1800 $cm^{-1}$. Equation 3 of Rahl et al. (2005), which is calibrated to their parameters R1 (the height ratio of D1/G) and R2 (the area ratio of D1/(G+D1+D2)), was utilized for 28 samples that yielded peak temperatures >400 °C. Equation 1 of Kouketsu et al. (2014), which is calibrated to the full width at half maximum of the D1 peak, was utilized for four samples that yielded peak temperatures <400 °C. Peak temperatures reported for our samples (Table 3) represent the mean of multiple analyzed grains of carbonaceous material (typically between 13 and 16 grains per sample). Peak temperatures are reported at a two standard error level, which accounts for internal uncertainty from our measurements and the external uncertainty from the calibration equations of Rahl et al. (2005) and Kouketsu et al. (2014) (see footnote of Table 3). Error ranges for our samples are typically on the order of ± 30–45 °C (Table 3; Fig. 6).

We analyzed 21 samples from the Salmon River transect, consisting of 13 from the western segment (Fig. 4A), two from the central segment (Fig. 4B), and six from the eastern segment (Fig. 4C). Samples ID20-10 and ID20-15 from the Heavens Gate thrust sheet yielded temperatures of 357 ± 20 °C and 359 ± 16 °C, respectively. Samples from the structurally imbricated Morrison Ridge thrust sheet (Fig. 4A) include four marble samples from the Martin Bridge Limestone (ID20-88, ID20-83, SR17A, and ID20-26), which yielded temperatures that increase moving structurally upward (384 ± 15 °C, 416 ± 44 °C, 424 ± 29 °C, and 498 ± 38 °C), and four phyllite samples from the Lucile Slate (SR18B, ID20-27,

[1]Supplemental Material. Consists of text that provides details on analytical methods for collection of Raman spectroscopy of carbonaceous material (RSCM) thermometry as well as two tables of supporting data for RSCM analyses. Please visit https://doi.org/10.1130/GEOS.S.22763711 to access the supplemental material, and contact editing@geosociety.org with any questions.

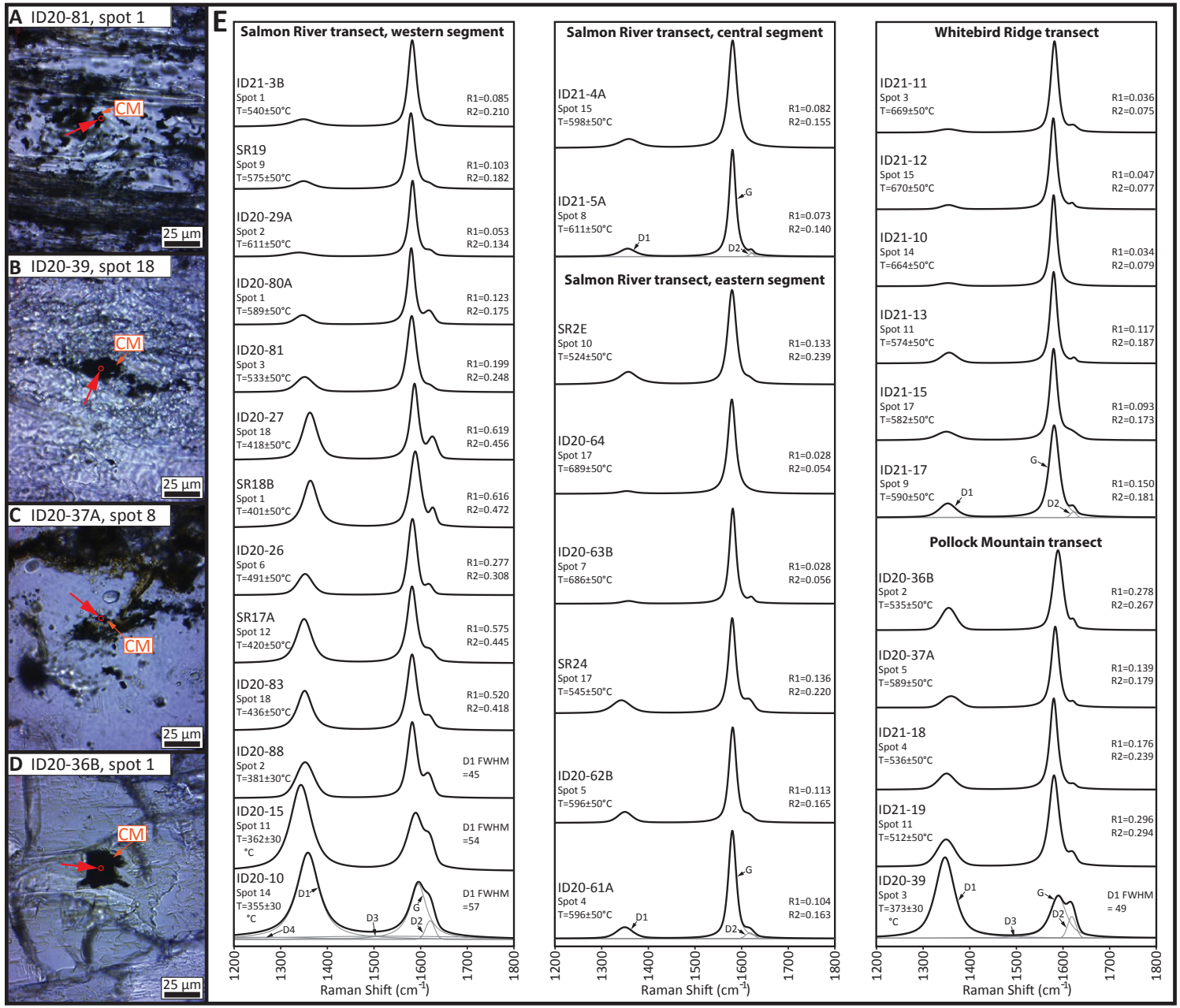


**Figure 6. (A–D): Photomicrographs (taken in plane-polarized light) of representative examples of analyzed grains of carbonaceous material (CM) from Salmon River suture zone samples. Red circles represent the approximate area of the analyzed spots. (E) Examples of representative Raman spectra from single grain analyses of each sample, organized in order of increasing structural position on each transect. Positions of the graphite peak G and defect peaks (D1–D4) are labeled on the bottom spectrum in each transect. Peak temperatures (T) for grain analyses >400 °C were calculated from Equation 3 of Rahl et al. (2005), and T for grain analyses ≤400 °C were calculated from Equation 1 of Kouketsu et al. (2014). Single grain analyses are listed with the external uncertainty of their corresponding calibration equation (±50 °C for Rahl et al., 2005, Equation 3, and ±30 °C for Kouketsu et al., 2014, Equation 1). R1 and R2 parameters are calculated after Rahl et al. (2005). FWHM—full width at half-maximum.**

TABLE 3. SUMMARY OF RAMAN SPECTROSCOPY OF CARBONACEOUS MATERIAL (RSCM) THERMOMETRY RESULTS FOR SALMON RIVER SUTURE ZONE SAMPLES

| Sample | Latitude | Longitude | Transect | Thrust sheet | Map unit | Lithology | Structural height (m) | Temperature calibration | D1 FWHM | | R1 | | R2 | | Peak temperature (˚C) | | | n |
|---|---|---|---|---|---|---|---|---|---|---|---|---|---|---|---|---|---|---|
| | | | | | | | | | Mean | 1σ | Mean | 1σ | Mean | 1σ | Mean | 1σ | 2 SE | |
| ID21-3B | 45.41297 | 116.31944 | Salmon River, western segment | Rapid River thrust sheet | TrJsc | schist | 4500 | Rahl et al. (2005) eq. 3 | — | — | 0.146 | 0.074 | 0.223 | 0.084 | 544 | 69 | 44 | 15 |
| SR19 | 45.40772 | 116.34134 | Salmon River, western segment | Rapid River thrust sheet | TrJsc | schist | 3725 | Rahl et al. (2005) eq. 3 | — | — | 0.129 | 0.059 | 0.190 | 0.060 | 574 | 46 | 36 | 14 |
| ID20-29A | 45.37069 | 116.37044 | Salmon River, western segment | Rapid River thrust sheet | Trlc | schist | 2925 | Rahl et al. (2005) eq. 3 | — | — | 0.069 | 0.037 | 0.149 | 0.070 | 600 | 64 | 45 | 13 |
| ID20-80A | 45.35519 | 116.39300 | Salmon River, western segment | Morrison Ridge thrust sheet | Trl | phyllite | 1900 | Rahl et al. (2005) eq. 3 | — | — | 0.100 | 0.044 | 0.154 | 0.060 | 604 | 54 | 36 | 17 |
| ID20-81 | 45.35492 | 116.39403 | Salmon River, western segment | Morrison Ridge thrust sheet | Trl | phyllite | 1875 | Rahl et al. (2005) eq. 3 | — | — | 0.196 | 0.074 | 0.243 | 0.062 | 537 | 45 | 32 | 18 |
| ID20-27 | 45.39830 | 116.41042 | Salmon River, western segment | Morrison Ridge thrust sheet | Trl | phyllite | 1850 | Rahl et al. (2005) eq. 3 | — | — | 0.426 | 0.150 | 0.403 | 0.071 | 427 | 48 | 33 | 18 |
| SR18B | 45.39048 | 116.42145 | Salmon River, western segment | Morrison Ridge thrust sheet | Trl | phyllite | 1800 | Rahl et al. (2005) eq. 3 | — | — | 0.587 | 0.088 | 0.459 | 0.045 | 407 | 31 | 30 | 16 |
| ID20-26 | 45.39442 | 116.41633 | Salmon River, western segment | Morrison Ridge thrust sheet | Trmb | marble | 1650 | Rahl et al. (2005) eq. 3 | — | — | 0.222 | 0.030 | 0.288 | 0.036 | 498 | 32 | 38 | 10 |
| SR17A | 45.38607 | 116.44364 | Salmon River, western segment | Morrison Ridge thrust sheet | Trmb | marble | 1525 | Rahl et al. (2005) eq. 3 | — | — | 0.594 | 0.139 | 0.445 | 0.051 | 424 | 26 | 29 | 15 |
| ID20-83 | 45.34861 | 116.40292 | Salmon River, western segment | Morrison Ridge thrust sheet | Trmb | marble | 1475 | Rahl et al. (2005) eq. 3 | — | — | 0.431 | 0.073 | 0.416 | 0.051 | 416 | 42 | 44 | 9 |
| ID20-88 | 45.34761 | 116.40453 | Salmon River, western segment | Morrison Ridge thrust sheet | Trmb | marble | 1450 | Kouketsu et al. (2014) eq. 1 | 43.6 | 2.1 | — | — | — | — | 384 | 5 | 15 | 16 |
| ID20-15 | 45.35972 | 116.49297 | Salmon River, western segment | Heavens Gate thrust sheet | Trws | phyllite | 1100 | Kouketsu et al. (2014) eq. 1 | 55.2 | 4.7 | — | — | — | — | 359 | 10 | 16 | 15 |
| ID20-10 | 45.36381 | 116.49794 | Salmon River, western segment | Heavens Gate thrust sheet | Trws | marble | 1075 | Kouketsu et al. (2014) eq. 1 | 56.1 | 12.8 | — | — | — | — | 357 | 28 | 20 | 17 |
| ID21-4A | 45.42183 | 116.28649 | Salmon River, central segment | Rapid River thrust sheet | TrJsc | schist | 3175 | Rahl et al. (2005) eq. 3 | — | — | 0.097 | 0.03 | 0.165 | 0.042 | 591 | 37 | 33 | 14 |
| ID21-5A | 45.41872 | 116.26678 | Salmon River, central segment | Rapid River thrust sheet | TrJsc | schist | 2250 | Rahl et al. (2005) eq. 3 | — | — | 0.092 | 0.06 | 0.147 | 0.077 | 609 | 64 | 41 | 16 |
| SR2E | 45.40183 | 116.10384 | Salmon River, eastern segment | Laurentian metasedimentary rocks | Zkm | paragneiss | 7900 | Rahl et al. (2005) eq. 3 | — | — | 0.151 | 0.036 | 0.246 | 0.043 | 522 | 39 | 32 | 16 |
| ID20-64 | 45.41131 | 116.18881 | Salmon River, eastern segment | Pollock Mountain thrust sheet | PTrp | schist | 1375 | Rahl et al. (2005) eq. 3 | — | — | 0.050 | 0.056 | 0.086 | 0.074 | 661 | 62 | 44 | 13 |
| ID20-63B | 45.40886 | 116.19119 | Salmon River, eastern segment | Rapid River thrust sheet | Trbc | schist | 1250 | Rahl et al. (2005) eq. 3 | — | — | 0.027 | 0.024 | 0.061 | 0.052 | 681 | 49 | 33 | 18 |
| SR24 | 45.40251 | 116.20014 | Salmon River, eastern segment | Rapid River thrust sheet | Trlc | schist | 875 | Rahl et al. (2005) eq. 3 | — | — | 0.144 | 0.017 | 0.221 | 0.026 | 546 | 24 | 32 | 12 |
| ID20-62B | 45.40172 | 116.20247 | Salmon River, eastern segment | Rapid River thrust sheet | Trlc | schist | 750 | Rahl et al. (2005) eq. 3 | — | — | 0.102 | 0.021 | 0.162 | 0.030 | 597 | 26 | 27 | 18 |
| ID20-61A | 45.39981 | 116.20906 | Salmon River, eastern segment | Rapid River thrust sheet | Pfc | schist | 500 | Rahl et al. (2005) eq. 3 | — | — | 0.109 | 0.023 | 0.167 | 0.031 | 593 | 27 | 28 | 16 |
| ID21-11 | 45.29034 | 116.36716 | Whitebird Ridge | Pollock Mountain thrust sheet | PTrp | schist | 2275 | Rahl et al. (2005) eq. 3 | — | — | 0.033 | 0.013 | 0.077 | 0.025 | 666 | 22 | 33 | 11 |
| ID21-12 | 45.29836 | 116.38136 | Whitebird Ridge | Pollock Mountain thrust sheet | PTrp | schist | 2175 | Rahl et al. (2005) eq. 3 | — | — | 0.043 | 0.024 | 0.075 | 0.037 | 671 | 32 | 33 | 13 |
| ID21-10 | 45.28899 | 116.36334 | Whitebird Ridge | Rapid River thrust sheet | TrJsc | schist | 2125 | Rahl et al. (2005) eq. 3 | — | — | 0.036 | 0.029 | 0.08 | 0.049 | 663 | 44 | 40 | 11 |
| ID21-13 | 45.29973 | 116.38188 | Whitebird Ridge | Rapid River thrust sheet | TrJsc | schist | 2100 | Rahl et al. (2005) eq. 3 | — | — | 0.118 | 0.056 | 0.186 | 0.069 | 575 | 58 | 48 | 10 |
| ID21-15 | 45.29932 | 116.40415 | Whitebird Ridge | Rapid River thrust sheet | TrJsc | phyllite | 2100 | Rahl et al. (2005) eq. 3 | — | — | 0.152 | 0.067 | 0.215 | 0.066 | 555 | 53 | 46 | 10 |
| ID21-17 | 45.29456 | 116.41005 | Whitebird Ridge | Rapid River thrust sheet | TrJsc | schist | 1925 | Rahl et al. (2005) eq. 3 | — | — | 0.132 | 0.07 | 0.18 | 0.079 | 585 | 64 | 41 | 16 |
| ID20-36B | 45.15669 | 116.46689 | Pollock Mountain | Rapid River thrust sheet | Pfc | schist | 925 | Rahl et al. (2005) eq. 3 | — | — | 0.222 | 0.029 | 0.252 | 0.022 | 536 | 18 | 34 | 10 |
| ID20-37A | 45.15769 | 116.47025 | Pollock Mountain | Morrison Ridge thrust sheet | Trl | phyllite | 825 | Rahl et al. (2005) eq. 3 | — | — | 0.135 | 0.050 | 0.177 | 0.058 | 590 | 49 | 33 | 18 |
| ID21-18 | 45.20474 | 116.44778 | Pollock Mountain | Morrison Ridge thrust sheet | Trl | phyllite | 700 | Rahl et al. (2005) eq. 3 | — | — | 0.198 | 0.08 | 0.251 | 0.068 | 529 | 51 | 37 | 15 |
| ID21-19 | 45.20869 | 116.44760 | Pollock Mountain | Morrison Ridge thrust sheet | Trmb | marble | 625 | Rahl et al. (2005) eq. 3 | — | — | 0.294 | 0.084 | 0.296 | 0.062 | 509 | 44 | 39 | 12 |
| ID20-39 | 45.16046 | 116.47629 | Pollock Mountain | Morrison Ridge thrust sheet | Trmb | marble | 575 | Kouketsu et al. (2014) eq. 1 | 49.0 | 2.1 | — | — | — | — | 373 | 4 | 17 | 13 |

*Notes:* See Figures 2 and 3 for a guide to unit abbreviations. Peak temperatures >400 °C were determined using equation 3 of Rahl et al. (2005) and peak temperatures between 200–400 °C were determined using equation 1 of Kouketsu et al. (2014). R1 and R2 parameters were calculated using equations 1 and 2 of Rahl et al. (2005), and D1 FWHM (full width at half maximum) values were calculated using procedures described in Kouketsu et al. (2014). Internal variability in R1, R2, D1 FWHM, and peak temperature is indicated by 1σ uncertainty. Peak temperatures are also reported at a 2 standard error (SE) level, calculated from quadratic addition of 1σ internal error and external error of ±50 ˚C from the Rahl et al. (2005) calibration or ±30 ˚C from the Kouketsu et al. (2014) equation 1 calibration, divided by the square root of the number of analyzed grains of carbonaceous material (n). Em dashes indicate no data.

ID20-81, and ID20-80), which also yielded temperatures that increase moving structurally upward (407 ± 30 °C, 427 ± 33 °C, 537 ± 32 °C, and 604 ± 36 °C). Five samples from the western and central portions of the Rapid River thrust sheet (ID20-29A, SR19, ID21-3B, ID21-5A, and ID21-4A) yielded temperatures of 600 ± 45 °C, 574 ± 36 °C, 544 ± 44 °C, 609 ± 41 °C, and 591 ± 33 °C, respectively (Figs. 4A and 4B). Four samples that are distributed across the uppermost 800 m of the Rapid River thrust sheet (ID20-61A, ID20-62B, SR24, and ID20-63B) yielded temperatures of 593 ± 28 °C, 597 ± 27 °C, 546 ± 32 °C, and 681 ± 33 °C, respectively (Fig. 4C). Sample ID20-64, which lies 50 m above the Pollock Mountain thrust, yielded 661 ± 44 °C. Sample SR2E, a schist of Laurentian affinity to the east of the $Sr_I$ ~0.706 isopleth, yielded 522 ± 32 °C.

We analyzed six samples from the Whitebird Ridge transect (Fig. 4D), including four samples that are distributed across the uppermost 225 m of the Rapid River thrust sheet (ID21-17, ID21-15, ID21-13, and ID21-10), which yielded temperatures of 585 ± 41 °C, 555 ± 46 °C, 575 ± 48 °C, and 663 ± 40 °C, and two samples from the basal 125 m of the Pollock Mountain thrust sheet (ID21-12: 671 ± 33 °C and ID21-11: 666 ± 33 °C). We analyzed five samples from the Pollock Mountain transect (Fig. 4E), consisting of four samples from the 0.4-km-thick Morrison Ridge thrust sheet (ID20-39, ID21-19, ID21-18, and ID20-37A), which yielded 373 ± 17 °C, 509 ± 39 °C, 529 ± 37 °C, and 590 ± 33 °C, and one sample from the Rapid River thrust sheet (ID20-36B: 536 ± 34 °C).

### 3.3. Approximate Deformation Temperatures from Quartz Recrystallization Microstructures

Assuming an invariant strain rate and constant water content during deformation, the dominant mechanism of dynamic recrystallization of quartz, which can be interpreted from visual analysis of recrystallized quartz in thin sections, can allow estimating approximate ranges of deformation temperature (e.g., Law, 2014). We observed microstructures characteristic of dynamic recrystallization of quartz in 47 thin sections from the Salmon River suture zone (Table 4). Three quartz recrystallization microstructures were observed: (1) ≤0.025-mm-diameter bulges or subgrains localized at the boundaries of detrital quartz clasts (Fig. 7A), which are indicative of bulging recrystallization (e.g., Bailey and Hirsch, 1962; Drury et al., 1985); (2) equigranular textures dominated by 0.05–0.1-mm-diameter quartz porphyroclasts (Figs. 7B–7F), which are indicative of subgrain rotation recrystallization (e.g., Poirier and Nicolas, 1975; White, 1977; Stipp et al., 2002); and (3) "amoeboid" quartz porphyroclasts up to 1–2 mm in diameter (Figs. 7G–7J), which are indicative of grain boundary migration recrystallization (e.g., Guillope and Poirier, 1979; Urai et al., 1986; Stipp et al., 2002). Our results are plotted on Figure 4, utilizing deformation temperatures that represent the full combined ranges measured by Stipp et al. (2002) for the Tonale fault zone in Italy and by Law (2014) for the Himalayan fold-thrust belt (~280–450 °C for bulging, ~400–550 °C for subgrain rotation, and ~500–700 °C for grain boundary migration). We interpret these deformation temperature ranges as approximate (e.g., Law, 2014), and we show them for qualitative comparison with our RSCM data and the thermobarometry data of Selverstone et al. (1992) and McKay et al. (2017).

Our quartz recrystallization observations define a pattern of increasing deformation temperature moving structurally upward and eastward through the suture zone. Bulging was observed in the basal part of the Heavens Gate thrust sheet (Fig. 4A). Subgrain rotation was observed in the uppermost 50 m of the Heavens Gate thrust sheet, distributed through the Morrison Ridge thrust sheet, and distributed through much of the Rapid River thrust sheet (Fig. 4). On the Salmon River transect, subgrain rotation transitions upward to grain boundary migration between 825 m and 575 m structural distance below the Pollock Mountain thrust, and grain boundary migration is dominant in all rocks to the east (Fig. 4C). On the Whitebird Ridge transect, the upward transition from subgrain rotation to grain boundary migration is between 25 m structurally below and 25 m structurally above the Pollock Mountain thrust (Fig. 4D). On the Pollock Mountain transect, grain boundary migration becomes dominant at 225–175 m structural distance below the Pollock Mountain thrust (Fig. 4E).

### 3.4. Integration and Summary of Metamorphic Temperature Data

To quantify peak temperature trends as a function of structural position, we combined all temperature data from the Salmon River transect onto one tectonostratigraphic column (Fig. 8A) and all temperature data from the Whitebird Ridge and Pollock Mountain transects onto another column (Fig. 8B). On both columns, the data illustrate a similar pattern of approximately isothermal conditions (i.e., no temperature trend with structural position) within individual ductile thrust sheets, which are separated by intervals of inverted temperatures (i.e., inverted thermal gradients) that are centered around the mapped positions of thrust faults.

On the Salmon River transect (Fig. 8A), rocks in the Heavens Gate thrust sheet yielded a mean peak temperature of 358 ± 18 °C (n = 2) (mean peak temperatures are reported with the mean error value of all individual samples, and thermal gradients were calculated using a linear regression and are reported with a 2σ error). Temperatures from six samples collected within the Morrison Ridge thrust sheet yielded a mean peak temperature of 426 ± 32 °C. Temperatures from two samples collected within a thin, overlying thrust sheet in the footwall of the Rapid River thrust increase upward from 537 ± 32 °C to 604 ± 36 °C; this increase defines a steep inverted thermal gradient of 1999 ± 616 °C/km. Sixteen samples distributed across the basal 3.1 km of the Rapid River thrust sheet yielded approximately isothermal temperatures, with a mean of 577 ± 30 °C. Structurally above this, between 450 m below and 50 m above the Pollock Mountain thrust, temperatures from six samples increase upward from 546 ± 32 °C to 681 ± 33 °C and are best-fit by an inverted thermal gradient of 242 ± 89 °C/km.

On the combined Whitebird Ridge/Pollock Mountain transect (Fig. 8B), temperatures from four samples that span the upper 275 m of the Morrison Ridge thrust sheet increase upward from 373 ± 17 °C to 590 ± 33 °C. When combined

TABLE 4. SUMMARY OF QUARTZ RECRYSTALLIZATION MECHANISM OBSERVATIONS FROM SALMON RIVER SUTURE ZONE THIN SECTIONS

| Sample | Latitude | Longitude | Transect | Thrust sheet | Map unit | Lithology | Structural height (m) | Quartz recrystallization mechanism |
|---|---|---|---|---|---|---|---|---|
| ID21-3B | 45.41297 | 116.31944 | Salmon River, western segment | Rapid River thrust sheet | TrJsc | Schist | 4500 | Subgrain rotation |
| SR19 | 45.40772 | 116.34134 | Salmon River, western segment | Rapid River thrust sheet | TrJsc | Schist | 3725 | Subgrain rotation |
| ID20-29A | 45.37069 | 116.37044 | Salmon River, western segment | Rapid River thrust sheet | Trlc | Schist | 2925 | Subgrain rotation |
| ID20-79 | 45.36561 | 116.38075 | Salmon River, western segment | Rapid River thrust sheet | Trlc | Schist | 2450 | Subgrain rotation |
| ID21-1 | 45.35519 | 116.39300 | Salmon River, western segment | Morrison Ridge thrust sheet | Trl | Phyllite | 1900 | Subgrain rotation |
| ID20-80A | 45.35519 | 116.39300 | Salmon River, western segment | Morrison Ridge thrust sheet | Trl | Phyllite | 1900 | Subgrain rotation |
| ID20-80B | 45.35519 | 116.39300 | Salmon River, western segment | Morrison Ridge thrust sheet | Trl | Quartzite | 1900 | Subgrain rotation |
| ID20-81 | 45.35492 | 116.39403 | Salmon River, western segment | Morrison Ridge thrust sheet | Trl | Phyllite | 1875 | Subgrain rotation |
| ID20-27 | 45.39830 | 116.41042 | Salmon River, western segment | Morrison Ridge thrust sheet | Trl | Slate | 1850 | Subgrain rotation |
| ID20-20A | 45.39094 | 116.45378 | Salmon River, western segment | Heavens Gate thrust sheet | Trws | Phyllite | 1400 | Subgrain rotation |
| ID20-86 | 45.33569 | 116.40642 | Salmon River, western segment | Heavens Gate thrust sheet | Trws | Volcaniclastic sandstone | 1375 | Subgrain rotation |
| SR15 | 45.34912 | 116.50961 | Salmon River, western segment | Heavens Gate thrust sheet | Trws | Argillite | 300 | Bulging |
| ID21-4A | 45.42183 | 116.28649 | Salmon River, central segment | Rapid River thrust sheet | TrJsc | Schist | 3175 | Subgrain rotation |
| ID21-5A | 45.41872 | 116.26678 | Salmon River, central segment | Rapid River thrust sheet | TrJsc | Schist | 2250 | Subgrain rotation |
| ID20-5 | 45.41242 | 116.25281 | Salmon River, central segment | Rapid River thrust sheet | Trbc | Amphibolite | 2025 | Subgrain rotation |
| SR12C | 45.39951 | 116.21679 | Salmon River, central segment | Rapid River thrust sheet | Trlc | Schist | 775 | Subgrain rotation |
| SR2E | 45.40183 | 116.10384 | Salmon River, eastern segment | Laurentian metasedimentary rocks | Zkm | Paragneiss | 7900 | Grain boundary migration |
| ID21-24 | 45.40092 | 116.11378 | Salmon River, eastern segment | Laurentian metasedimentary rocks | Zkm | Schist | 7150 | Grain boundary migration |
| ID20-71B | 45.42651 | 116.13518 | Salmon River, eastern segment | Laurentian metasedimentary rocks | Zkm | Quartzite | 5100 | Grain boundary migration |
| SR5A | 45.42680 | 116.13590 | Salmon River, eastern segment | Intrusive rocks | PKv | Orthogneiss | 5000 | Grain boundary migration |
| SR5B | 45.42680 | 116.13590 | Salmon River, eastern segment | Intrusive rocks | PKv | Orthogneiss | 5000 | Grain boundary migration |
| SR21 | 45.41667 | 116.16844 | Salmon River, eastern segment | Pollock Mountain thrust sheet | Trk | Schist | 2775 | Grain boundary migration |
| SR8C | 45.41873 | 116.17146 | Salmon River, eastern segment | Pollock Mountain thrust sheet | Trk | Orthogneiss | 2425 | Grain boundary migration |
| ID20-67B | 45.41883 | 116.17164 | Salmon River, eastern segment | Pollock Mountain thrust sheet | Trk | Orthogneiss | 2375 | Grain boundary migration |
| ID20-65 | 45.41244 | 116.18719 | Salmon River, eastern segment | Pollock Mountain thrust sheet | PTrp | Orthogneiss | 1550 | Grain boundary migration |
| ID20-64 | 45.41131 | 116.18881 | Salmon River, eastern segment | Pollock Mountain thrust sheet | PTrp | Schist | 1375 | Grain boundary migration |
| ID20-63B | 45.40886 | 116.19119 | Salmon River, eastern segment | Rapid River thrust sheet | Trbc | Schist | 1250 | Grain boundary migration |
| SR10E | 45.40260 | 116.19970 | Salmon River, eastern segment | Rapid River thrust sheet | Trlc | Schist | 900 | Grain boundary migration |
| SR24 | 45.40251 | 116.20014 | Salmon River, eastern segment | Rapid River thrust sheet | Trlc | Schist | 875 | Grain boundary migration |
| ID20-62B | 45.40172 | 116.20247 | Salmon River, eastern segment | Rapid River thrust sheet | Trlc | Schist | 750 | Grain boundary migration |
| ID20-61B | 45.39981 | 116.20906 | Salmon River, eastern segment | Rapid River thrust sheet | Pfc | Quartzite | 500 | Subgrain rotation |
| ID21-12 | 45.29836 | 116.38136 | Whitebird Ridge | Pollock Mountain thrust sheet | PTrp | Schist | 2175 | Grain boundary migration |
| ID21-10 | 45.28899 | 116.36334 | Whitebird Ridge | Rapid River thrust sheet | TrJsc | Schist | 2125 | Subgrain rotation |
| ID21-13 | 45.29973 | 116.38188 | Whitebird Ridge | Rapid River thrust sheet | TrJsc | Schist | 2100 | Subgrain rotation |
| ID21-14 | 45.31306 | 116.39399 | Whitebird Ridge | Rapid River thrust sheet | TrJsc | Calcareous schist | 2100 | Subgrain rotation |
| ID21-15 | 45.29932 | 116.40415 | Whitebird Ridge | Rapid River thrust sheet | TrJsc | Phyllite | 2100 | Subgrain rotation |
| ID21-17 | 45.29456 | 116.41005 | Whitebird Ridge | Rapid River thrust sheet | TrJsc | Schist | 1925 | Subgrain rotation |
| ID20-32C | 45.20114 | 116.40847 | Pollock Mountain | Pollock Mountain thrust sheet | Trdg | Orthogneiss | 1600 | Grain boundary migration |
| ID21-20 | 45.20780 | 116.43665 | Pollock Mountain | Rapid River thrust sheet | TrJsc | Schist | 1150 | Subgrain rotation |
| ID20-53 | 45.15642 | 116.46131 | Pollock Mountain | Rapid River thrust sheet | Pfc | Schist | 1075 | Grain boundary migration |
| ID20-35 | 45.15778 | 116.46406 | Pollock Mountain | Rapid River thrust sheet | Pfc | Amphibolite | 1000 | Subgrain rotation |
| ID20-56 | 45.15619 | 116.46558 | Pollock Mountain | Rapid River thrust sheet | Pfc | Amphibolite | 950 | Grain boundary migration |
| ID20-36A | 45.15669 | 116.46689 | Pollock Mountain | Rapid River thrust sheet | Pfc | Schist | 925 | Subgrain rotation |
| ID20-36B | 45.15669 | 116.46689 | Pollock Mountain | Rapid River thrust sheet | Pfc | Schist | 925 | Subgrain rotation |
| ID20-37A | 45.15769 | 116.47025 | Pollock Mountain | Morrison Ridge thrust sheet | Trl | Phyllite | 825 | Subgrain rotation |
| ID21-18 | 45.20474 | 116.44778 | Pollock Mountain | Morrison Ridge thrust sheet | Trl | Phyllite | 700 | Subgrain rotation |
| ID21-19 | 45.20869 | 116.4476 | Pollock Mountain | Morrison Ridge thrust sheet | Trmb | Marble | 625 | Subgrain rotation |

*Notes:* See Figures 2 and 3 for a guide to unit abbreviations.

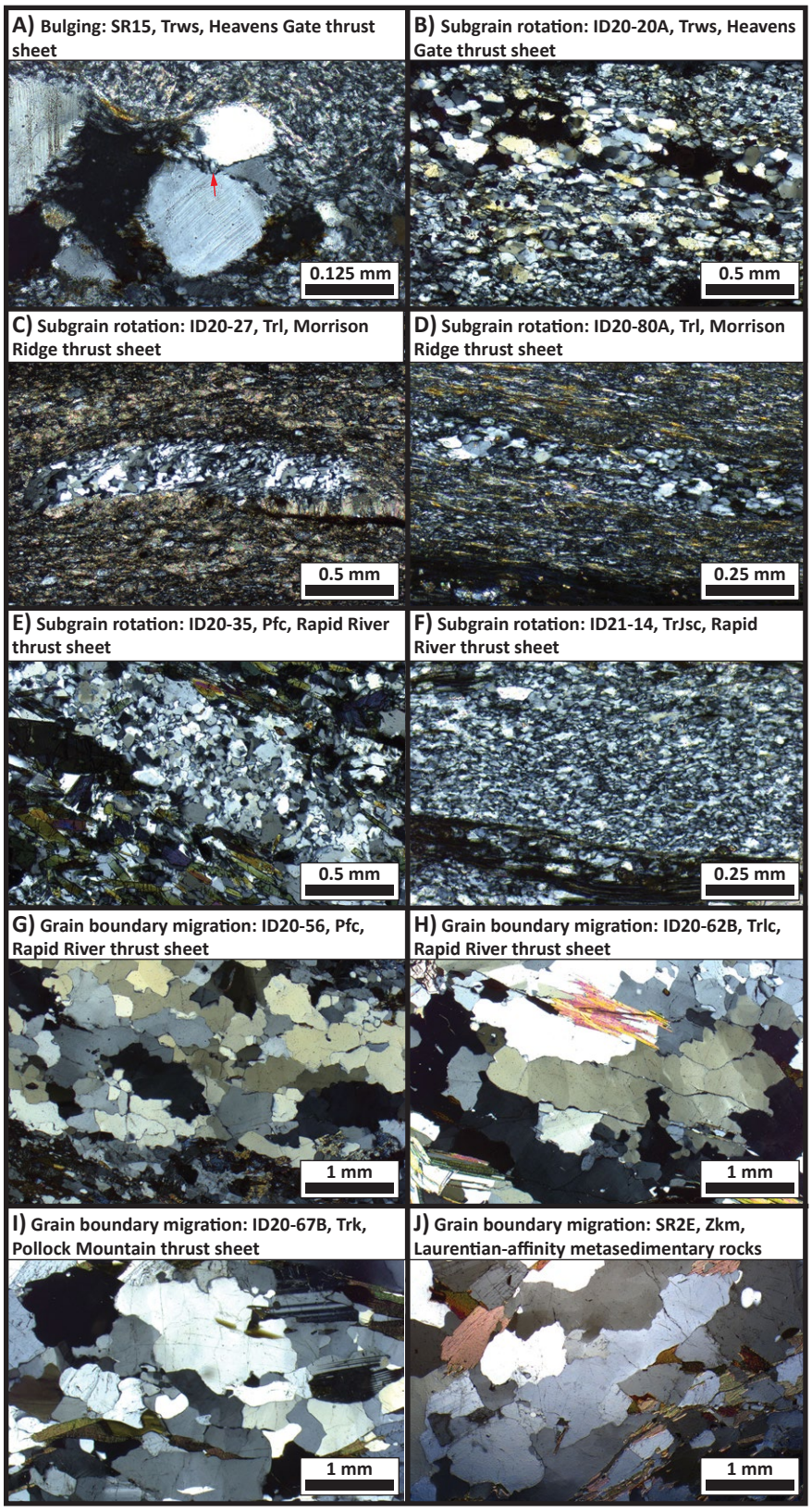


**Figure 7. Photomicrographs (taken in cross-polarized light) of representative quartz recrystallization microstructures in thin sections from the Salmon River suture zone, organized from structurally low (A) to high (J). See Figures 2 and 3 for a guide to rock unit abbreviations. (A) Bulges and subgrains (≤0.025-mm-diameter) localized along the boundaries of adjacent detrital quartz clasts, characteristic of bulging recrystallization. (B–F) Equigranular texture of ~0.05–0.1-mm-diameter quartz porphyroclasts, characteristic of subgrain rotation recrystallization. (G–J) Interfingering "amoeboid" quartz porphyroclasts up to ~1–2 mm in diameter, characteristic of grain boundary migration recrystallization.**

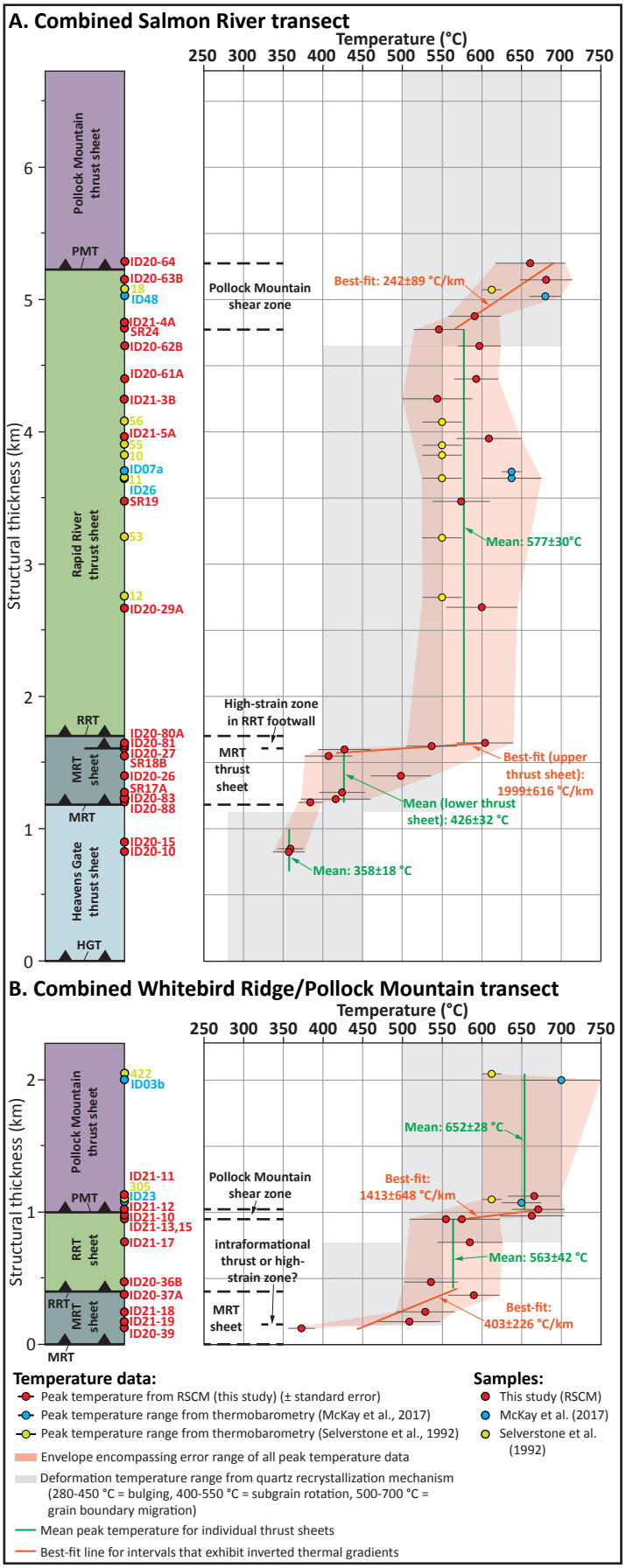


**Figure 8. Tectonostratigraphic columns of: (A) the combined Salmon River transect, which includes temperature data from the western, central, and eastern segments (an approximate error of ±25 °C was used for the six temperature samples of Selverstone et al., 1992, from the Rapid River thrust sheet); and (B) the combined Whitebird Ridge and Pollock Mountain transects, which include all temperature data collected from both transects. Temperature data are graphed versus structural thickness to the right of each column and include our Raman spectroscopy of carbonaceous material (RSCM) temperatures, published thermobarometry from Selverstone et al. (1992) and McKay et al. (2017), and general deformation temperature patterns defined by our quartz recrystallization observations. Interpretations of the spatial extent of the Pollock Mountain shear zone (graphs A and B), a high-strain zone within the footwall of the Rapid River thrust (graph A), and a possible intraformational thrust or high-strain zone (graph B) within the Morrison Ridge thrust sheet are shown. Abbreviations: HGT—Heavens Gate thrust; MRT—Morrison Ridge thrust; PMT—Pollock Mountain thrust; RRT—Rapid River thrust.**

with sample ID20-36B (75 m above the Rapid River thrust), these five samples are best-fit by an inverted thermal gradient of 403 ± 226 °C/km. In the Rapid River thrust sheet, temperatures between 75 m above the Rapid River thrust and 50 m below the Pollock Mountain thrust are approximately isothermal, with a mean temperature of 563 ± 42 °C (n = 4). Between 50 m below and 25 m above the Pollock Mountain thrust, four samples are best-fit by a steep inverted thermal gradient of 1413 ± 648 °C/km. Between 25 m and 1150 m above the Pollock Mountain thrust, temperatures from six samples do not exhibit a trend with structural position and yielded a mean temperature of 652 ± 28 °C.

## 4. DISCUSSION

The data summarized above define a pattern of approximately isothermal conditions within individual ~1–3-km-thick, penetratively deformed thrust sheets in the western portion of the Salmon River suture zone, which are separated by ~100–500-m-thick inverted thermal gradients that surround the mapped positions of thrust faults. We interpret that this portion of the suture zone represents a ductile accretionary complex, which evolved via in-sequence accretion and top-to-the-west translation of ductile thrust sheets that were deformed at progressively lower temperatures and depths with time (e.g., Pavlis, 1986; Dunlap et al., 1997). When viewed in the context of the thermal regime of folded isotherms produced during arc-continent collision (Fig. 9A) (e.g., Vogt et al., 2012; Vogt and Gerya, 2014; Dymkova et al., 2016; Yang et al., 2018), this "ductile accretionary complex" interpretation for the Salmon River suture zone can explain several first-order aspects of its thermal and structural architecture, including: (1) the genesis of inverted thermal gradients that are localized across the mapped positions of thrust faults, (2) the approximately isothermal conditions distributed within individual ductile thrust sheets, (3) the stepwise decrease in the mean peak temperatures of ductile thrust sheets moving structurally downward and westward, and (4) the published metamorphic and exhumation histories of the Pollock Mountain and Rapid River thrust sheets.

This discussion is supported by Figure 9, a series of schematic cross sections that illustrate increments of the structural evolution of the Salmon River suture zone. On Figure 9, we interpret the construction of the ductile accretionary complex in the western part of the Salmon River suture zone as the consequence of east-directed, A-type (i.e., Alpine- or Ampferer-type; Bally, 1975) subduction of the eastern portion of the Wallowa island arc terrane during its accretion with North America. This interpretation is supported by receiver function imaging ~120 km to the south, which defines a shallowly east-dipping, mid-crustal reflector to the east of the western Idaho shear zone. This reflector is interpreted to represent the shear zone along which accreted terranes of the Blue Mountains Province were partially subducted eastward beneath North American crust (Stanciu et al., 2016).

Steady-state isotherms from a thermal model of collisional orogenesis from Henry et al. (1997) are shown on Figures 9A and 9B. The folding of isotherms at and below the subduction interface, which becomes more pronounced at greater depths, is an inherent feature of thermal-mechanical models of collisional orogenic systems (e.g., Henry et al., 1997; Huerta et al., 1998; Herman et al., 2010; Jamieson and Beaumont, 2013; Vogt et al., 2012; Vogt and Gerya, 2014; Dymkova et al., 2016; Yang et al., 2018). At mid-crustal depths (starting at ~15 km on Figs. 9A and 9B), low to near-isothermal gradients are predicted beneath the subduction interface, which can explain the isothermal peak temperatures distributed within ductile thrust sheets of the Salmon River suture zone. Within this mid-crustal thermal regime, top-to-the-west displacement that juxtaposed hanging wall rocks that record higher peak temperatures over footwall rocks that record lower peak temperatures can explain the origin of inverted thermal gradients across thrust faults (e.g., Corrie and Kohn, 2011; Long et al., 2016). Accordingly, we interpret that the spatial limits of the inverted thermal gradients that we document in the Salmon River suture zone likely define high-strain zones of ductile shearing in which the majority of differential top-to-the-west displacement was localized (e.g., Long et al., 2016; Grujic et al., 2020). Therefore, although all structural levels of the thrust sheets in the suture zone were penetratively sheared during their burial, accretion, and translation, with thrust-subparallel linear-planar fabrics likely indicating a component of transport-parallel stretching (e.g., Means, 1989), we interpret that the majority of top-to-the-west translation was accommodated within relatively narrow (~100–500-m-thick) high-strain zones of ductile, thrust-sense shearing. Additionally, we acknowledge that shear heating (e.g., Pavlis, 1986; Molnar and England, 1990) likely also played a role in the attainment of the peak temperatures that we document in the ductile thrust sheets of the suture zone, as penetrative ductile fabrics are observed at all structural levels.

The earliest event in the Salmon River suture zone that is attributed to accretion of the Wallowa terrane was the ca. 144–123 Ma prograde metamorphism of rocks that presently comprise the Pollock Mountain thrust sheet (Figs. 9A and 9B) (Getty et al., 1993; McKay et al., 2017). These rocks were buried to peak depths of ~29–37 km (assuming a lithostatic pressure gradient of 3.7 km/kbar; Table 2) and a mean peak temperature of 652 ± 28 °C (Fig. 8B) prior to their accretion and translation above the Pollock Mountain thrust, which is interpreted to have initiated between ca. 121–117 Ma based on the timing of exhumation-related cooling through ~500 °C (Fig. 9C) (Lund and Snee, 1988; Snee et al., 1995; McKay et al., 2017). Ductile fabrics and top-to-the-west shear-sense indicators are spatially distributed in both the hanging wall and footwall of the mapped position of the Pollock Mountain thrust (e.g., Blake, 1991; Blake et al., 2009; McKay et al., 2017; Gray et al., 2020), and pressure-temperature-time data indicate that displacement on this structure juxtaposed rocks in its hanging wall and footwall at mid-crustal depths (Selverstone et al., 1992). Therefore, we find it more appropriate to view the Pollock Mountain "thrust" as a thrust-sense ductile shear zone. On the Salmon River transect, we document an inverted thermal gradient that spans between 450 m below and 50 m above the mapped position of the Pollock Mountain thrust (Fig. 8A), and on the Whitebird Ridge/Pollock Mountain transects, the inverted thermal gradient spans from 50 m below to 25 m above the mapped position of the

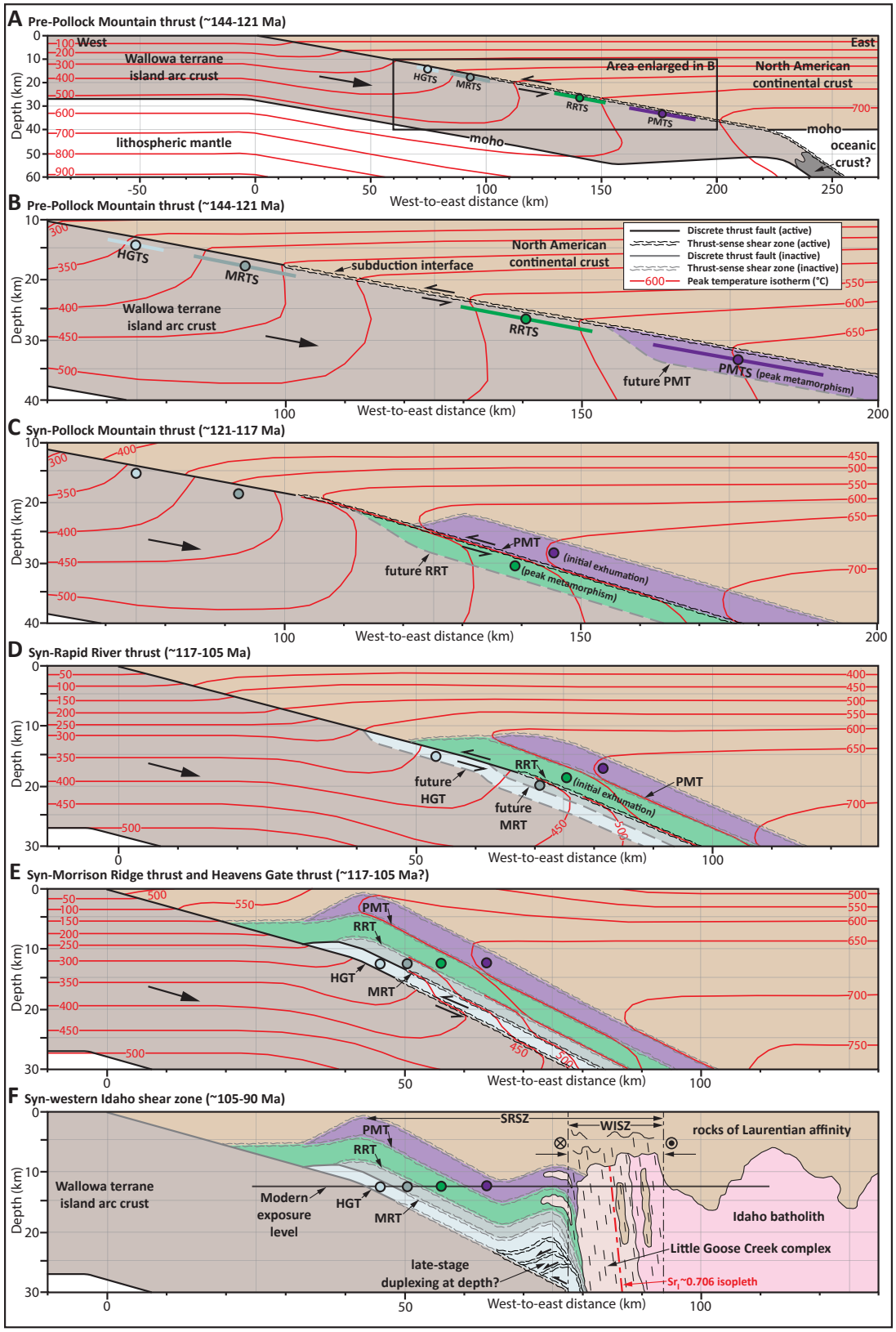


**Figure 9. Schematic cross-section diagrams depicting the structural evolution of the Salmon River suture zone (SRSZ). See text Sections 2 and 4 for discussion of published timing constraints. (A) Initial underthrusting (i.e., A-type subduction of Bally, 1975) of the eastern portion of the Wallowa terrane. The relative positions of rocks within four future ductile thrust sheets are shown (PMTS—Pollock Mountain thrust sheet; RRTS—Rapid River thrust sheet; MRTS—Morrison Ridge thrust sheet; HGTS—Heavens Gate thrust sheet) and are plotted based on the mean peak temperatures that they will eventually attain. Mean peak temperatures (dots) and error ranges (thick lines extending from dots) for individual thrust sheets from Figure 8 are plotted. Steady-state isotherms are from Model 1 of Henry et al. (1997; their fig. 5). The 26 km crustal thickness shown for the Wallowa terrane is from Tetreault and Buiter (2014). The 10° eastward-dipping initial subduction angle that is shown is consistent with a shallowly east-dipping, mid-crustal reflector ~120 km to the south that is interpreted as the subduction interface between Blue Mountains Province terranes and North American crust (Stanciu et al., 2016). In order to account for the published constraints on the burial depths of ductile thrust sheets, Laurentian-affinity rocks are shown overlying the suture zone accretionary complex on the west. (B) Enlarged portion of cross section A. (C) Geometry after displacement on the Pollock Mountain thrust (PMT). For cross sections C–E, the temperature error ranges for the ductile thrust sheets are no longer shown for simplicity, and schematic isotherms represent the peak temperature conditions recorded at any given structural level, which locally may have been attained prior to the time increment shown in each cross section. (D) Geometry after displacement on the Rapid River thrust (RRT). Note the change in west-to-east position and depth relative to cross section C. (E) Geometry after displacement on the Morrison Ridge thrust (MRT) and Heavens Gate thrust (HGT). (F) Geometry after ca. 105–90 Ma (timing range from Giorgis et al., 2008) dextral-transpressional shearing in the western Idaho shear zone (WISZ), which overprinted the eastern portion of the SRSZ and generated steeply east-dipping ductile fabrics. Late-stage duplexing is hypothesized at depth, as a mechanism to construct the long-wavelength folds observed on the Salmon River transect (the Riggins synform and Lake Creek antiform). The approximate paleodepth of the modern exposure level is shown. The 25° final eastward dip that is shown for ductile thrust sheets in the western part of the suture zone is supported by the modern ~20°–30° range of eastward dips for the Heavens Gate, Morrison Ridge, and Rapid River thrusts on the Salmon River transect (Fig. 2).**

thrust (Fig. 8B). We interpret that these intervals of inverted temperatures approximately demarcate the lower and upper boundaries of high-strain, top-to-the-west ductile shearing accommodated within the Pollock Mountain shear zone (e.g., Long et al., 2016).

Rocks within the Rapid River thrust sheet experienced prograde metamorphism between ca. 130–111 Ma (McKay et al., 2017; Gray et al., 2020) and achieved a peak depth range of ~28–32 km (Table 2) (Selverstone et al., 1992; McKay et al., 2017) and a mean peak temperature of 577 ± 30 °C (Fig. 8A). The timing of prograde metamorphism of the Rapid River thrust sheet overlaps with the ca. 121–117 Ma initial exhumation-related cooling of the overlying Pollock Mountain thrust sheet, which McKay et al. (2017) interpreted as evidence for the in-sequence westward progression of thrust-related burial and exhumation in the Salmon River suture zone (Fig. 9C). The accretion and initiation of top-to-the-west translation of the Rapid River thrust sheet is dated by exhumation-related cooling through ~500 °C as early as ca. 117 Ma in the western portion of the thrust sheet and between ca. 111–105 Ma in the central portion (Selverstone et al., 1992; McKay et al., 2017) (Fig. 9D).

Along the Salmon River transect, mean peak temperatures increase upward across the Morrison Ridge thrust from ~358 °C to ~426 °C (Fig. 8A). Above this, temperatures increase upward from ~427 °C to ~604 °C within a thin thrust sheet in the footwall of the Rapid River thrust, defining a steep inverted thermal gradient (Fig. 8A). The presence of multiple thrust sheets between the Morrison Ridge and Rapid River thrusts that exhibit upward-increasing peak temperatures is compatible with progressive footwall imbrication within an east-dipping, top-to-the-west thrust zone (Figs. 9D and 9E). The significant temperature increase in the footwall of the Rapid River thrust could be the consequence of displacement on an unmapped thrust fault within the Lucile Slate or distributed top-to-the-west simple shear within a high-strain zone of ductile shearing within the Lucile Slate. Telescoping of isotherms within this interval may have also been aided by lineation-parallel stretching and foliation-normal thinning, which has been documented within portions of the Rapid River and Heavens Gate thrust sheets using measurements of outcrop-scale stretched clasts (Aliberti, 1988; Blake, 1991; Gray et al., 2020). Regardless of the specific style of strain, we interpret that the 150-m-thick thrust sheet in the footwall of the Rapid River thrust on the Salmon River transect is a high-strain zone that accomplished significant differential top-to-the-west displacement (Fig. 8A).

On the Pollock Mountain transect, peak temperatures collected from the 400-m-thick Morrison Ridge thrust sheet increase upward, with the lowest sample yielding ~373 °C and the highest three samples yielding a mean of ~542 °C (Fig. 8B). The significant upward increase in metamorphic temperature between these two domains, which are only separated by 50 m structural distance, may be the consequence of internal thrust imbrication within the Morrison Ridge thrust sheet, perhaps along an unmapped, intraformational top-to-the-west thrust fault within the Martin Bridge Limestone. Alternatively, distributed top-to-the-west simple shear and/or thrust-subnormal thinning (e.g., Aliberti, 1988; Blake, 1991; Gray et al., 2020) may have also contributed to the telescoping of isotherms within this package. Regardless of the specific geometric scenario, the upward increase from ~373 °C at the base of this package to an average of ~563 °C in the overlying Rapid River thrust sheet (Fig. 8B) suggests that the 400-m-thick Morrison Ridge thrust sheet is also likely a high-strain zone that accomplished significant top-to-the-west displacement on the Pollock Mountain transect.

The Heavens Gate thrust demarcates the basal structural level of penetrative ductile fabrics in the Salmon River suture zone (Gray and Oldow, 2005; Gray et al., 2020). Gray et al. (2020) documented that displacement on the Heavens Gate thrust postdated ca. 136 Ma intrusion of diorite in its hanging wall. Additionally, Casares et al. (2021) dated diorite dikes that intrude rocks beneath the Heavens Gate thrust, which experienced greenschist-facies metamorphism along with the country rocks that they intruded. The youngest two of these dikes yielded U-Pb zircon crystallization ages of 120 ± 1.0 Ma, which constrain the maximum age of burial-related metamorphism of the footwall of the Heavens Gate thrust. On the basis of this field relationship, we suggest that displacement on the Heavens Gate thrust is ca. 120 Ma or younger. Based on the ~358 °C mean peak temperature of the Heavens Gate thrust sheet (Fig. 8A), accretion may have taken place at depths as shallow as ~10–20 km (Figs. 9D and 9E).

In summary, we interpret the stacked series of penetratively deformed thrust sheets in the western portion of the Salmon River suture zone as a ductile accretionary complex (e.g., Pavlis, 1986; Dunlap et al., 1997) that records the progressive underplating of ductile thrust sheets that were transferred to the North American plate from the leading edge of the Wallowa terrane during Early Cretaceous (ca. 144–105 Ma) A-type subduction. We interpret the stepwise decrease in peak temperatures moving structurally downward and westward as the consequence of stacking of thrust sheets at progressively shallower depths with time during accretion, which started at ~30–35 km depths (Pollock Mountain thrust sheet) and completed at depths likely as shallow as ~10–20 km (Heavens Gate thrust sheet) (Figs. 9B–9E). Whether or not this system is a true ductile duplex versus a ductile imbricate system depends on whether the up-dip portions of individual thrust faults were emergent at the time of their displacement (e.g., Boyer and Elliott, 1982), which is unknown. However, given the considerable depth at which they were emplaced, we consider it likely that the Salmon River suture zone developed as a ductile duplex system.

Following (or perhaps partially overlapping with) (Gray et al., 2020) the construction of the ductile accretionary complex, dextral transpressional shearing on the western Idaho shear zone between ca. 105–90 Ma (timing range from Giorgis et al., 2008) overprinted the eastern portion of the suture zone (e.g., McClelland et al., 2000; Tikoff et al., 2001; Giorgis et al., 2008) (Figs. 1 and 9F). Deformation in the western Idaho shear zone generated steeply east-dipping, linear-planar ductile fabrics, and is interpreted to have accomplished northward translation of the accreted rocks to its west and significant (perhaps as much as ~100 km), internal east-west shortening (Giorgis and Tikoff, 2004; Giorgis et al., 2005). Late-stage duplexing may have taken place at depth beneath the central portion of the Salmon River suture zone, either prior to or during dextral transpressional shearing (e.g., Blake et al., 2009), as a possible mechanism to

construct the long-wavelength folds on the Salmon River transect (the Riggins synform and Lake Creek antiform) (Fig. 9F). Alternatively, these folds could be the consequence of a westward-decreasing strain gradient associated with the east-west shortening accomplished in the western Idaho shear zone.

## 5. CONCLUSIONS

(1) Penetratively deformed, 1–3-km-thick ductile thrust sheets in the western portion of the Salmon River suture zone exhibit isothermal peak temperatures, which decrease moving structurally downward from ~650 °C (Pollock Mountain thrust sheet), to ~575 °C (Rapid River thrust sheet), to ~425 °C (Morrison Ridge thrust sheet), to ~360 °C (Heavens Gate thrust sheet).

(2) We interpret the western portion of the Salmon River suture zone as a ductile accretionary complex that records the progressive underplating and top-to-the-west translation of ductile thrust sheets derived from the Wallowa island arc terrane during its Early Cretaceous (ca. 144–105 Ma) collision with North America. Accretion of thrust sheets initiated at depths of ~30–35 km and completed at depths likely as shallow as ~10–20 km.

(3) Ductile thrust sheets in the accretionary complex are separated by 100–500-m-thick intervals of inverted temperatures that surround the mapped positions of thrust faults. We interpret that these intervals delineate the approximate spatial limits of zones of high-strain ductile shearing in which the majority of top-to-the-west, thrust-sense displacement was accommodated.


### ACKNOWLEDGMENTS

This work was supported by National Science Foundation (NSF)-EAR 2015601 awarded to Sean Long and NSF-EAR 2015604 awarded to Matthew McKay. We acknowledge the use of facilities within the Eyring Materials Center at Arizona State University, which is supported in part by NNCI-ECCS-2025490. We thank Reed Lewis, Keith Gray, and John Watkinson for spending time in the field, discussing Salmon River suture zone geology and inspiring several of the ideas presented here. We would also like to thank Adelie Ionescu and Ray Eckland for assistance during field work. Reviews by Basil Tikoff, an anonymous reviewer, and Associate Editor Terry Pavlis significantly improved this paper. The manuscript and data repository contain all of the data used for this research.


### REFERENCES CITED


Aliberti, E.A., 1988, A structural, petrographic, and isotopic study of the Rapid River area and selected mafic complexes in the Northwestern United States: Implications for evolution of an abrupt island arc-continent boundary [Ph.D. dissertation]: Cambridge, Massachusetts, Harvard University, 194 p.

Allmendinger, R.W., 1992, Fold and thrust tectonics of the western United States exclusive of the accreted terranes, *in* Burchfiel, B.C., Lipman, P.W., and Zoback, M.L., eds., The Cordilleran Orogen: Conterminous U.S.: Boulder, Colorado, Geological Society of America, Geology of North America, v. G-3, p. 583–608, https://doi.org/10.1130/DNAG-GNA-G3.583.

Armstrong, R.L., Taubeneck, W.H., and Hales, P.O., 1977, Rb-Sr and K-Ar geochronometry of Mesozoic granitic rocks and their Sr-isotopic composition: Oregon, Washington, and Idaho: Geological Society of America Bulletin, v. 88, no. 3, p. 397–411, https://doi.org/10.1130/0016-7606(1977)88<397:RAKGOM>2.0.CO;2.

Avé Lallemant, H.G., 1995, Pre-Cretaceous tectonic evolution of the Blue Mountains province, northeastern Oregon, *in* Vallier, T.L., and Brooks, H.C., eds., Geology of the Blue Mountains Region of Oregon, Idaho, and Washington; Petrology and Tectonic Evolution of Pre-Tertiary Rocks of the Blue Mountains Region: U.S. Geological Survey Professional Paper 1438, p. 359–414.

Bailey, J.E., and Hirsch, P.B., 1962, The recrystallization process in some polycrystalline metals: Proclamations of the Royal Society of London, serial A267, p. 11–30.

Bally, A.W., 1975, A geodynamic scenario for hydrocarbon occurrences: Tokyo, 9th World Petrological Congress, v. 2, p. 23–44.

Beaumont, C., Jamieson, R.A., Nguyen, M.H., and Lee, B., 2001, Himalayan tectonics explained by extrusion of a low-viscosity crustal channel coupled to focused surface denudation: Nature, v. 414, p. 738–742, https://doi.org/10.1038/414738a.

Beaumont, C., Jamieson, R.A., Nguyen, M.H., and Medvedev, S., 2004, Crustal channel flows: 1. Numerical models with applications to the tectonics of the Himalayan-Tibetan orogen: Journal of Geophysical Research, v. 109, B06406, https://doi.org/10.1029/2003JB002809.

Beyssac, O., Goffe, B., Chopin, C., and Rouzaud, J., 2002, Raman spectra of carbonaceous material in metasediments: A new geothermometer: Journal of Metamorphic Geology, v. 20, p. 859–871, https://doi.org/10.1046/j.1525-1314.2002.00408.x.

Beyssac, O., Goffe, B., Petitet, J.P., Froigneux, E., Moreau, M., and Rouzaud, J.N., 2003, On the characterization of disordered and heterogeneous carbonaceous materials by Raman spectroscopy: Spectrochimica Acta Part A, v. 59, p. 2267–2276, https://doi.org/10.1016/S1386-1425(03)00070-2.

Blake, D.E., 1991, Geology of the Western Idaho Suture Zone in the Salmon River Gorge, West-Central Idaho [Ph.D. dissertation]: Pullman, Washington, Washington State University, 330 p.

Blake, D.E., Gray, K.D., Giorgis, S., and Tikoff, B., 2009, A tectonic transect through the Salmon River suture zone along the Salmon River Canyon in the Riggins region of west-central Idaho, *in* O'Conner, J.E., Dorsey, R.J., and Madin, I.P., eds., Volcanoes to Vineyards: Geologic Field Trips through the Dynamic Landscape of the Pacific Northwest: Geological Society of America Field Guide 15, p. 345–372, https://doi.org/10.1130/2009.fld015(18).

Blake, D.E., Bruce, M.L., and Reed, D.N., 2016, Geologic Map of the Riggins Hot Springs Quadrangle and Adjacent Areas, Idaho County, Idaho: Idaho Geological Survey Geologic Map 53, scale 1:24,000.

Bollen, E.M., 2015, Explaining discontinuous garnet zoning using reaction history P-T models: an example from the Salmon River suture zone, west central Idaho [M.S. thesis]: Tuscaloosa, Alabama, University of Alabama, 103 p.

Bollinger, L., Avouac, J.P., Beyssac, O., Catlos, E.J., Harrison, T.M., Grove, M., Goffe, B., and Sapkota, S., 2004, Thermal structure and exhumation history of the Lesser Himalaya in central Nepal: Tectonics, v. 23, TC5015, https://doi.org/10.1029/2003TC001564.

Boyer, S.E., and Elliott, D., 1982, Thrust systems: The American Association of Petroleum Geologists Bulletin, v. 66, p. 1196–1230.

Braudy, N., Gaschnig, R.M., Wilford, D., Vervoort, J.D., Nelson, C.L., Davidson, C., Kahn, M.J., and Tikoff, B., 2017, Timing and deformation conditions of the western Idaho shear zone, West Mountain, west-central Idaho: Lithosphere, v. 9, no. 2, p. 157–183, https://doi.org/10.1130/L519.1.

Burchfiel, B.C., and Davis, G.A., 1972, Structural framework and evolution of the southern part of the Cordilleran orogen, western United States: American Journal of Science, v. 272, p. 97–118, https://doi.org/10.2475/ajs.272.2.97.

Burchfiel, B.C., and Davis, G.A., 1975, Nature and controls of Cordilleran orogenesis, western United States—Extension of an earlier synthesis: American Journal of Science, v. 275A, p. 363–396.

Burchfiel, B.C., Cowan, D.S., and Davis, G.A., 1992, Tectonic overview of the Cordilleran orogen in the western United States, *in* Burchfiel, B.C., Lipman, P.W., and Zoback, M.L., eds., The Cordilleran Orogen, Conterminous U.S.: Boulder, Colorado, Geological Society of America, Geology of North America, v. G-3, p. 407–479, https://doi.org/10.1130/DNAG-GNA-G3.407.

Buseck, P.R., and Huang, B.J., 1985, Conversion of carbonaceous material to graphite during metamorphism: Geochimica et Cosmochimica Acta, v. 49, no. 10, p. 2003–2016, https://doi.org/10.1016/0016-7037(85)90059-6.

Casares, H.L., Nicholson, K.N., and Malone, S.J., 2021, Evolution of the Seven Devils volcanic arc and period of amalgamation with the North American Craton based on zircon U/Pb geochronology and Hf isotope geochemistry of intrusions in the Seven Devils Mountains, western Idaho (USA): Geotectonics, v. 55, no. 2, p. 293–306, https://doi.org/10.1134/S0016852121020035.

Coney, P.J., Jones, D.L., and Monger, J.W.H., 1980, Cordilleran suspect terranes: Nature, v. 288, p. 329–333, https://doi.org/10.1038/288329a0.

Corrie, S.L., and Kohn, M.J., 2011, Metamorphic history of the central Himalaya, Annapurna region, Nepal, and implications for tectonic models: Geological Society of America Bulletin, v. 123, no. 9–10, p. 1863–1879, https://doi.org/10.1130/B30376.1.

Criss, R.E., and Fleck, R.J., 1987, Petrogenesis, geochronology, and hydrothermal systems of the northern Idaho batholith and adjacent areas based on $^{18}O/^{16}O$, $^{87}Sr/^{86}Sr$, K-Ar, and $^{40}Ar/^{39}Ar$ studies, *in* Vallier, T.L., and Brooks, H.C., eds., Geology of the Blue Mountains Region of Oregon, Idaho, and Washington: The Idaho Batholith and Its Border Zone: U.S. Geological Survey Professional Paper 1436, 44 p.

Dahl, P.S., 1996, The effects of composition on retentivity of argon and oxygen in hornblende and related amphiboles: A field-based empirical model: Geochimica et Cosmochimica Acta, v. 60, p. 3687–3700, https://doi.org/10.1016/0016-7037(96)00170-6.

Dahlen, F.A., 1990, Critical taper model of fold-and-thrust belts and accretionary wedges: Annual Review of Earth and Planetary Sciences, v. 18, p. 55–99, https://doi.org/10.1146/annurev.ea.18.050190.000415.

Dahlstrom, C.D.A., 1969, Balanced cross-sections: Canadian Journal of Earth Sciences, v. 6, p. 743–757, https://doi.org/10.1139/e69-069.

Davis, D., Suppe, J., and Dahlen, F.A., 1983, Mechanics of fold-and-thrust belts and accretionary wedges: Journal of Geophysical Research, v. 88, p. 1153–1172, https://doi.org/10.1029/JB088iB02p01153.

DeCelles, P.G., 2004, Late Jurassic to Eocene evolution of the Cordilleran thrust belt and foreland basin system, western U.S.A: American Journal of Science, v. 304, p. 105–168, https://doi.org/10.2475/ajs.304.2.105.

DeYoung, D.G., 2019, Geologic mapping and geochronology of the Heaven's Gate 7.5-minute quadrangle: How long does it take to accrete an island arc to a continent? [M.S. thesis]: Springfield, Missouri, Missouri State University, 75 p.

Dickinson, W.R., 2004, Evolution of the North American Cordillera: Annual Review of Earth and Planetary Sciences, v. 32, p. 13–45, https://doi.org/10.1146/annurev.earth.32.101802.120257.

Dickinson, W.R., 2008, Accretionary Mesozoic–Cenozoic expansion of the Cordilleran continental margin in California and adjacent Oregon: Geosphere, v. 4, no. 2, p. 329–353, https://doi.org/10.1130/GES00105.1.

Drury, M.R., Humphreys, F.J., and White, S.H., 1985, Large strain deformation studies using polycrystalline magnesium as rock analogue, Part II: Dynamic recrystallization mechanisms at high temperatures: Physics of the Earth and Planetary Interiors, v. 40, p. 208–222, https://doi.org/10.1016/0031-9201(85)90131-1.

Dunlap, W.J., Hirth, G., and Teyssier, C., 1997, Thermomechanical evolution of a ductile duplex: Tectonics, v. 16, no. 6, p. 983–1000, https://doi.org/10.1029/97TC00614.

Dymkova, D., Gerya, T., and Burg, J.-P., 2016, 2D thermomechanical modelling of continent-arc-continent collision: Gondwana Research, v. 32, p. 138–150, https://doi.org/10.1016/j.gr.2015.02.012.

Edelman, S.H., and Sharp, W.D., 1989, Terranes, early faults, and pre-Late Jurassic amalgamation of the western Sierra Nevada metamorphic belt, California: Geological Society of America Bulletin, v. 101, no. 11, p. 1420–1433, https://doi.org/10.1130/0016-7606(1989)101<1420:TEFAPL>2.3.CO;2.

Ernst, W.G., Snow, C.A., and Scherer, H.H., 2008, Contrasting early and late Mesozoic petrotectonic evolution of northern California: Geological Society of America Bulletin, v. 120, no. 1–2, p. 179–194, https://doi.org/10.1130/B26173.1.

Evenchick, C.A., McMechan, M.E., McNicoll, V.J., and Carr, S.D., 2007, A synthesis of the Jurassic–Cretaceous tectonic evolution of the central and southeastern Canadian Cordillera: Exploring links across the orogen, *in* Sears, J.W., Harms, T.A., and Evenchick, C.A., eds., Whence the Mountains? Inquiries into the Evolution of Orogenic Systems: A Volume in Honor of Raymond A. Price: Geological Society of America Special Paper 433, p. 117–145.

Fleck, R.J., and Criss, R.E., 1985, Strontium and oxygen isotopic variations in Mesozoic and Tertiary plutons of central Idaho: Contributions to Mineralogy and Petrology, v. 90, p. 291–308, https://doi.org/10.1007/BF00378269.

Fleck, R.J., and Criss, R.E., 2004, Location, age, and tectonic significance of the Western Idaho Suture Zone (WISZ): U.S. Geological Survey Open-File Report 2004-1039, 48 p., https://doi.org/10.3133/ofr20041039.

Fossen, H., and Tikoff, B., 1993, The deformation matrix for simultaneous simple shearing, pure shearing and volume change, and its application to transpression-transtension tectonics: Journal of Structural Geology, v. 15, p. 413–422, https://doi.org/10.1016/0191-8141(93)90137-Y.

Gaschnig, R.M., Vervoort, J.D., Lewis, R.S., and McClelland, W.C., 2010, Migrating magmatism in the northern U.S. Cordillera: In situ U-Pb geochronology of the Idaho batholith: Contributions to Mineralogy and Petrology, v. 159, no. 6, p. 863–883, https://doi.org/10.1007/s00410-009-0459-5.

Getty, S.R., Selverstone, J., Wernicke, B.P., Jacobsen, S.B., Aliberti, E.A., and Lux, D.R., 1993, Sm-Nd dating of multiple garnet growth events in an arc-continent collision zone, northwestern U.S. Cordillera: Contributions to Mineralogy and Petrology, v. 115, p. 45–57, https://doi.org/10.1007/BF00712977.

Giorgis, S., and Tikoff, B., 2004, Constraints on kinematics and strain from feldspar porphyroclast populations, *in* Alsop, G.I., Holdsworth, R.E., McCaffrey, K.J.W., and Hand, M., eds., Flow Processes in Faults and Shear Zones: Geological Society of London Special Publication 224, p. 265–285, https://doi.org/10.1144/GSL.SP.2004.224.01.17.

Giorgis, S., Tikoff, B., and McClelland, W., 2005, Missing Idaho arc: Transpressional modification of the $^{87}Sr/^{86}Sr$ transition on the western edge of the Idaho batholith: Geology, v. 33, no. 6, p. 469–472, https://doi.org/10.1130/G20911.1.

Giorgis, S., McClelland, W., Fayon, A., Singer, B.S., and Tikoff, B., 2008, Timing of deformation and exhumation in the western Idaho shear zone, McCall, Idaho: Geological Society of America Bulletin, v. 120, no. 9–10, p. 1119–1133, https://doi.org/10.1130/B26291.1.

Goodwin, L.B., and Tikoff, B., 2002, Competency contrast, kinematics, and the development of foliations and lineations in the crust: Journal of Structural Geology, v. 24, no. 6–7, p. 1065–1085, https://doi.org/10.1016/S0191-8141(01)00092-X.

Gray, K.D., 2013a, Structure of the arc-continent transition in the Riggins region of west-central Idaho—Fabric element strip map (West): Hells Canyon–Seven Devils Mountains-Little Salmon River: Idaho Geological Survey Technical Report 13-1, scale 1:24,000, 1 plate.

Gray, K.D., 2013b, Structure of the arc-continent transition in the Riggins region of west-central Idaho—Fabric element strip map (East): Little Salmon River–Riggins–Salmon River Canyon: Idaho Geological Survey Technical Report 13-1, scale 1:24,000, 1 plate.

Gray, K.D., and Isakson, V.H., 2016, Age, setting, and tectonic significance of the Fish Hatchery stock: Lower Rapid River canyon, west-central Idaho: Geological Society of America Abstracts with Programs, v. 48, no. 6, https://doi.org/10.1130/abs/2016RM-275975.

Gray, K.D., and Oldow, J.S., 2005, Contrasting structural histories of the Salmon River belt and Wallowa terrane: Implications for terrane accretion in northeastern Oregon and west-central Idaho: Geological Society of America Bulletin, v. 117, no. 5–6, p. 687–706, https://doi.org/10.1130/B25411.1.

Gray, K.D., Isakson, V., Schwartz, D., and Vervoort, J.D., 2020, Orogenic link ~41°N–46°N: Collisional mountain building and basin closure in the Cordillera of western North America: Geosphere, v. 16, no. 1, p. 136–181, https://doi.org/10.1130/GES02074.1.

Grujic, D., Ashley, K.T., Coble, M.A., Coutand, I., Kellett, D.A., Larson, K.P., Whipp, D.M., Jr., Gao, M., and Whynot, M., 2020, Deformational temperatures across the Lesser Himalayan Sequence in Eastern Bhutan and their implications for the deformation history of the Main Central Thrust: Tectonics, v. 39, no. 4, https://doi.org/10.1029/2019TC005914.

Guillope, M., and Poirier, J.P., 1979, Dynamic recrystallization during creep of single-crystalline halite: An experimental study: Journal of Geophysical Research, v. 84, p. 5557–5567, https://doi.org/10.1029/JB084iB10p05557.

Hamilton, W., 1963, Metamorphism in the Riggins region, western Idaho: U.S. Geological Society Professional Paper 436, 95 p., https://doi.org/10.3133/pp436.

Hamilton, W., 1969, Reconnaissance Geologic Map of the Riggins Quadrangle, West-Central Idaho: U.S. Geological Survey Miscellaneous Geologic Investigations Map I-579, scale 1:250,000.

Henry, P., Le Pichon, X.L., and Goffé, B., 1997, Kinematic, thermal and petrological model of the Himalayas: Constraints related to metamorphism within the underthrust Indian crust and topographic elevation: Tectonophysics, v. 273, p. 31–56, https://doi.org/10.1016/S0040-1951(96)00287-9.

Herman, F., Copeland, P., Avouac, J.-P., Bollinger, L., Mahéo, G., Le Fort, P., Rai, S., Foster, D., Pêcher, A., Stüwe, K., and Henry, P., 2010, Exhumation, crustal deformation, and thermal structure of the Nepal Himalaya derived from inversion of thermochronological and thermobarometric data and modeling of the topography: Journal of Geophysical Research, v. 115, B06407, https://doi.org/10.1029/2008JB006126.

Huerta, A.D., Royden, L.H., and Hodges, K.V., 1998, The thermal structure of collisional orogens as a response to accretion, erosion, and radiogenic heating: Journal of Geophysical Research, v. 103, p. 15,287–15,302, https://doi.org/10.1029/98JB00593.

Jamieson, R.A., and Beaumont, C., 2013, On the origin of orogens: Geological Society of America Bulletin, v. 125, no. 11–12, p. 1671–1702, https://doi.org/10.1130/B30855.1.

Jones, D.L., Siberling, N.J., and Hillhouse, J., 1977, Wrangellia—A displaced terrane in northwestern North America: Canadian Journal of Earth Sciences, v. 14, p. 2565–2577, https://doi.org/10.1139/e77-222.

Kauffman, J.D., Schmidt, K.L., Lewis, R.S., Stewart, D.E., Othberg, K.L., and Garwood, D.L., 2014, Geologic Map of the Idaho Part of the Grangeville 30×60 Minute Quadrangle, and Adjoining Areas of Washington and Oregon: Idaho Geological Survey Geologic Map 50, scale 1:100,000.

Kohn, M.J., 2014, Himalayan metamorphism and its tectonic implications: Annual Review of Earth and Planetary Sciences, v. 42, p. 381–419, https://doi.org/10.1146/annurev-earth-060313-055005.

Kouketsu, Y., Mizukami, T., Mori, H., Endo, S., Aoya, M., Hara, H., and Wallis, S., 2014, A new approach to develop the Raman carbonaceous material geothermometer for low-grade metamorphism using peak width: The Island Arc, v. 23, p. 33–50, https://doi.org/10.1111/iar.12057.

LaMaskin, T.A., Vervoot, J.D., Dorsey, R.J., and Wright, J.E., 2011, Early Mesozoic paleogeography and tectonic evolution of the western United States: Insights from detrital zircon U-Pb geochronology, Blue Mountains Province, northeastern Oregon: Geological Society of America Bulletin, v. 123, no. 9–10, p. 1939–1965, https://doi.org/10.1130/B30260.1.

LaMaskin, T.A., Dorsey, R.J., Vervoort, J.D., Schmitz, M.D., Tumpane, K.P., and Moore, N.O., 2015, Westward growth of Laurentia by pre-Late Jurassic terrane accretion, eastern Oregon and western Idaho, United States: The Journal of Geology, v. 123, no. 9–10, p. 233–267, https://doi.org/10.1086/681724.

Law, R.D., 2014, Deformation thermometry based on quartz c-axis fabrics and recrystallization microstructures: A review: Journal of Structural Geology, v. 66, p. 129–161, https://doi.org/10.1016/j.jsg.2014.05.023.

Long, S.P., Gordon, S.M., Young, J.P., and Soignard, E., 2016, Temperature and strain gradients through Lesser Himalayan rocks and across the Main Central thrust, south-central Bhutan: implications for transport-parallel stretching and inverted metamorphism: Tectonics, v. 35, p. 1863–1891, https://doi.org/10.1002/2016TC004242.

Lund, K., 1984, Tectonic history of a continent-island arc boundary, west-central Idaho [Ph.D. dissertation]: University Park, Pennsylvania, Pennsylvania State University, 207 p.

Lund, K., 2004, Geology of the Payette National Forest and vicinity, west-central Idaho (ver. 1.1, April 2021): U.S. Geological Survey Professional Paper 1666-A, 1666-B, 89 p., https://doi.org/10.3133/pp1666.

Lund, K., and Snee, L.W., 1988, Metamorphism, structural development, and age of the continent-island arc juncture in west-central Idaho, *in* Ernst, W.G., ed., Metamorphism and Crustal Evolution of the Western United States: Rubey Volume 7: Englewood Cliffs, New Jersey, Prentice Hall, p. 296–331.

Lünsdorf, N.K., Dunkl, I., Schmidt, B.C., Rantitsch, G., and von Eynatten, H., 2017, Towards a higher comparability of geothermometric data obtained by Raman spectroscopy of carbonaceous material. Part 2: A revised geothermometer: Geostandards and Geoanalytical Research, v. 41, no. 4, p. 593–612, https://doi.org/10.1111/ggr.12178.

Manduca, C.A., Silver, L.T., and Taylor, L.T., 1992, $^{87}Sr/^{86}Sr$ and $^{19}O/^{16}O$ isotopic systematics and geochemistry of granitoid plutons across a steeply-dipping boundary between contrasting lithospheric blocks in western Idaho: Contributions to Mineralogy and Petrology, v. 109, p. 355–372, https://doi.org/10.1007/BF00283324.

Manduca, C.A., Kuntz, M.A., and Silver, L.T., 1993, Emplacement and deformation history of the western margin of the Idaho batholith near McCall, Idaho: Influence of a major terrane boundary: Geological Society of America Bulletin, v. 105, no. 6, p. 749–765, https://doi.org/10.1130/0016-7606(1993)105<0749:EADHOT>2.3.CO;2.

Mann, A., 2018, Age and Structure of the Fish Hatchery Stock; Lower Rapid River Canyon, Riggins Region of West-Central Idaho [M.S. thesis]: Wichita, Kansas, Wichita State University, 79 p.

McClelland, W.C., Gehrels, G.E., and Saleeby, J.B., 1992, Upper Jurassic–Lower Cretaceous basinal strata along the Cordilleran margin: Implications for the accretionary history of the Alexander-Wrangellia–Peninsular terrane: Tectonics, v. 11, p. 823–835, https://doi.org/10.1029/92TC00241.

McClelland, W.C., Tikoff, B., and Manduca, C.A., 2000, Two-phase evolution of accretionary margins: Examples from the North American Cordillera: Tectonophysics, v. 326, p. 37–55, https://doi.org/10.1016/S0040-1951(00)00145-1.

McKay, M.P., 2011, Pressure-temperature-time paths, prograde garnet growth, and protolith of tectonites from a polydeformational, polymetamorphic terrane: Salmon River suture zone, west-central Idaho [M.S. thesis]: Tuscaloosa, Alabama, University of Alabama, 135 p.

McKay, M.P., Stowell, H.H., Gray, K.D., Schwartz, J.J., and Bollen, E., 2017, Metamorphism records thrust faulting during prolonged terrane accretion: Sm-Nd garnet and U-Pb zircon geochronology and P-T paths from the Salmon River suture zone, west-central Idaho: Lithosphere, v. 9, no. 5, p. 683–701, https://doi.org/10.1130/L642.1.

Means, W.D., 1989, Stretching faults: Geology, v. 17, no. 10, p. 893–896, https://doi.org/10.1130/0091-7613(1989)017<0893:SF>2.3.CO;2.

Means, W.D., 1994, Rotational quantities in homogeneous flow and the development of small-scale structures: Journal of Structural Geology, v. 17, p. 893–896.

Mitra, G., 1994, Strain variation in thrust sheets across the Sevier fold-and-thrust belt (Idaho-Utah-Wyoming): Implications for section restoration and wedge taper evolution: Journal of Structural Geology, v. 16, p. 585–602, https://doi.org/10.1016/0191-8141(94)90099-X.

Molnar, P., and England, P., 1990, Temperatures, heat flux, and frictional stress near major thrust faults: Journal of Geophysical Research, v. 95, p. 4833–4856, https://doi.org/10.1029/JB095iB04p04833.

Monger, J.W.H., Price, R.A., and Tempelman-Kluit, D.J., 1982, Tectonic accretion and the origin of the two major metamorphic and plutonic welts in the Canadian Cordillera: Geology, v. 10, no. 2, p. 70–75, https://doi.org/10.1130/0091-7613(1982)10<70:TAATOO>2.0.CO;2.

Montz, W.J., and Kruckenberg, S.C., 2017, Cretaceous partial melting, deformation, and exhumation of the Potters Pond migmatite domain, west-central Idaho: Lithosphere, v. 9, no. 2, p. 205–222, https://doi.org/10.1130/L555.1.

Nandi, S.K., Brown, M.B., DeYoung, S., McKay, M.P., Sage, M., and Spurgeon, D., 2018, Geologic map and cross sections of the Pollock Mountain 7.5-minute quadrangle, Idaho and Adams Counties, Idaho: National Cooperative Geologic Mapping Program EDMAP program, scale 1:24,000, 1 plate, accessed from the National Geologic Map Database on 10 October 2021.

Nelson, J.L., Colpron, M., and Israel, S., 2013, Chapter 3: The Cordillera of British Columbia, Yukon, and Alaska: Tectonics and Metallogeny: Society of Economic Geologists Special Publication 17, p. 53–109.

Oldow, J.S., Bally, A.W., Avé Lallemant, H.G., and Leeman, W.P., 1989, Phanerozoic evolution of the North American Cordillera: United States and Canada, *in* Bally, A.W., and Palmer, A.R., eds., The Geology of North America—An Overview: Boulder, Colorado, Geological Society of America, Geology of North America, v. A, p. 139–232, https://doi.org/10.1130/DNAG-GNA-A.139.

Onasch, C.M., 1977, Structural evolution of the western margin of the Idaho batholith in the Riggins, Idaho, area [Ph.D. dissertation]: University Park, Pennsylvania, Pennsylvania State University, 196 p.

Onasch, C.M., 1987, Temporal and spatial relations between folding, intrusion, metamorphism, and thrust faulting in the Riggins area, west-central Idaho, *in* Vallier, T.L., and Brooks, H.C., eds., Geology of the Blue Mountains Region of Oregon, Idaho, and Washington: The Idaho Batholith and Its Border Zone: U.S. Geological Survey Professional Paper 1436, p. 139–149.

Pavlis, T.L., 1986, The role of strain heating in the evolution of megathrusts: Journal of Geophysical Research: Solid Earth, v. 91, p. 12,407–12,422, https://doi.org/10.1029/JB091iB12p12407.

Poirier, J.P., and Nicolas, A., 1975, Deformation-induced recrystallization by progressive misorientation of subgrain-boundaries, with special reference to mantle peridotites: The Journal of Geology, v. 83, no. 6, p. 707–720, https://doi.org/10.1086/628163.

Powell, R., and Holland, T., 1994, Optimal geothermometry and geobarometry: The American Mineralogist, v. 79, p. 120–133.

Price, R.A., 1981, The Cordilleran foreland thrust and fold belt in the southern Canadian Rocky Mountains, *in* McClay, K.R., and Price, N.J., eds., Thrust and Nappe Tectonics: Geological Society of London Special Publication 9, p. 427–448, https://doi.org/10.1144/GSL.SP.1981.009.01.39.

Rahl, J.M., Anderson, K.M., Brandon, M.T., and Fassoulas, C., 2005, Raman spectroscopic carbonaceous material thermometry of low-grade metamorphic rocks: Calibration and application to tectonic exhumation in Crete, Greece: Earth and Planetary Science Letters, v. 240, p. 339–354, https://doi.org/10.1016/j.epsl.2005.09.055.

Ramsay, J.G., 1969, The measurement of strain and displacement in orogenic belts, *in* Kent, P.E., Satterthwaite, G.E., and Spencer, A.M., eds., Time and Place in Orogeny: Geological Society of London Special Publication 3, p. 43–79, https://doi.org/10.1144/GSL.SP.1969.003.01.04.

Riddell, J., 2011, Lithostratigraphic and tectonic framework of Jurassic and Cretaceous Intermontane sedimentary basins of south-central British Columbia: Canadian Journal of Earth Sciences, v. 48, p. 870–896, https://doi.org/10.1139/e11-034.

Rusmore, M.E., Potter, C.J., and Umhoefer, P.J., 1988, Middle Jurassic terrane accretion along the western edge of the Intermontane superterrane, southwestern British Columbia: Geology, v. 16, no. 10, p. 891–894, https://doi.org/10.1130/0091-7613(1988)016<0891:MJTAAT>2.3.CO;2.

Sanderson, D.J., 1982, Models of strain variation in nappes and thrust sheets: A review: Tectonophysics, v. 88, p. 201–233, https://doi.org/10.1016/0040-1951(82)90237-2.

Sarewitz, D., 1982, Geology of part of the Heavens Gate quadrangle, Seven Devils Mountains, western Idaho [M.S. thesis]: Corvallis, Oregon, Oregon State University, 144 p.

Schmidt, K.L., Gray, K.D., Lewis, R.S., Steven, C.J., and Isakson, V.H., 2016, Mesozoic tectonics west of the accretionary boundary in west-central Idaho: A road log along U.S. Highway 95 between Moscow and New Meadows, Idaho, *in* Lewis, R.S., and Schmidt, K.L., eds., Exploring the Geology of the Inland Northwest: Geological Society of America Field Guide 41, p. 175–209, https://doi.org/10.1130/2016.0041(06).

Schwartz, J.J., Snoke, A.W., Frost, C.D., Barnes, C.G., Gromet, L.P., and Johnson, K., 2010, Analysis of the Wallowa-Baker terrane boundary: Implications for tectonic accretion in the Blue Mountains Province, northeastern Oregon: Geological Society of America Bulletin, v. 122, no. 3–4, p. 517–536, https://doi.org/10.1130/B26493.1.

Selverstone, J., Wernicke, B.P., and Aliberti, E.A., 1992, Intracontinental subduction and hinged unroofing along the Salmon River suture zone, west central Idaho: Tectonics, v. 11, p. 124–144, https://doi.org/10.1029/91TC02418.

Silberling, N.J., Jones, D.L., Blake, M.C., Jr., and Howell, D.G., 1984, Lithotectonic terrane map of the western conterminous United States, *in* Silberling, N.J., and Jones, D.L., eds., Lithotectonic terrane maps of the North American Cordillera: U.S. Geological Survey Open-File Report 84-523, 43 p.

Snee, L.W., Lund, K., Sutter, J.F., Balcer, D.E., and Evans, K.V., 1995, An $^{40}Ar/^{39}Ar$ chronicle of the tectonic development of the Salmon River suture zone, western Idaho, *in* Vallier, T.L., and Brooks, H.C., eds., Geology of the Blue Mountains Region of Oregon, Idaho, and Washington: Petrology and Tectonic Evolution of Pre-Tertiary Rocks of the Blue Mountains Region: U.S. Geological Survey Professional Paper 1438, p. 359–414.

Stanciu, A.C., Russo, R.M., Mocanu, V.I., Bremner, P.M., Hongsresawat, S., Torpey, M.E., VanDecar, J.C., Foster, D.A., and Hole, J.A., 2016, Crustal structure beneath the Blue Mountains terranes and cratonic North America, eastern Oregon, and Idaho, from teleseismic receiver functions: Journal of Geophysical Research: Solid Earth, v. 121, no. 7, p. 5049–5067, https://doi.org/10.1002/2016JB012989.

Stipp, M., Stunitz, H., Heilbronner, R., and Schmid, S.M., 2002, The eastern Tonale fault zone: A 'natural laboratory' for crystal plastic deformation over a temperature range from 250° to 700°C: Journal of Structural Geology, v. 24, p. 1861–1884, https://doi.org/10.1016/S0191-8141(02)00035-4.

Tetreault, J.L., and Buiter, S.J.H., 2014, Future accreted terranes: A compilation of island arcs, oceanic plateaus, submarine ridges, seamounts, and continental fragments: Solid Earth, v. 5, p. 1243–1275, https://doi.org/10.5194/se-5-1243-2014.

Tikoff, B., Kelso, P., Manduca, C., Markley, M.J., and Gillaspy, J., 2001, Lithospheric and crustal reactivation of an ancient plate boundary: The assembly and disassembly of the Salmon River suture zone, Idaho, USA, *in* Holdsworth, R.E., Strachan, R.A., Magloughlin, J.F., and Knipe, R.J., eds., The Nature and Tectonic Significance of Fault Zone Weakening: Geological Society of London Special Publication 186, p. 213–231, https://doi.org/10.1144/GSL.SP.2001.186.01.13.

Unruh, D.M., Lund, K., Kuntz, M.A., and Snee, L.W., 2008, Uranium-lead zircon ages and Sr, Nd, and Pb isotope geochemistry of selected plutonic rocks from western Idaho: U.S. Geological Survey Open-File Report 2008-1142, 37 p., https://doi.org/10.3133/ofr20081142.

Urai, J.L., Means, W.D., and Lister, G.S., 1986, Dynamic recrystallization of minerals, *in* Hobbs, B.E., and Heard, H.C., eds., Mineral and Rock Deformation: Laboratory Studies: Washington, D.C., American Geophysical Union Geophysical Monograph 36, p. 161–199, https://doi.org/10.1029/GM036p0161.

Vallier, T.L., 1977, The Permian and Triassic Seven Devils Group, Western Idaho and Northeastern Oregon: U.S. Geological Survey Bulletin 1437, 55 p.

Vallier, T.L., 1995, Petrology of pre-Tertiary igneous rocks in the Blue Mountains region of Oregon, Idaho, and Washington: Implications for the geologic evolution of a complex island arc, *in* Vallier, T.L., and Brooks, H.C., eds., Geology of the Blue Mountains Region of Oregon, Idaho, and Washington: U.S. Geological Survey Professional Paper 1438, p. 125–209.

Vogt, K., and Gerya, T.V., 2014, From ocean plateaus to allochthonous terranes: Numerical modeling: Gondwana Research, v. 25, p. 494–508, https://doi.org/10.1016/j.gr.2012.11.002.

Vogt, K., Gerya, T.V., and Castro, A., 2012, Crustal growth at active continental margins: numerical modeling: Physics of the Earth and Planetary Interiors, v. 192, p. 1–20, http://doi.org/10.1016/j.pepi.2011.12.003.

White, S., 1977, Geological significance of recovery and recrystallization processes in quartz: Tectonophysics, v. 39, p. 143–170, https://doi.org/10.1016/0040-1951(77)90093-2.

Wyld, S.J., and Wright, J.E., 2001, New evidence for Cretaceous strike-slip faulting in the United States Cordillera and implications for terrane displacement, deformation patterns, and plutonism: American Journal of Science, v. 301, p. 150–181, https://doi.org/10.2475/ajs.301.2.150.

Yang, S.-H., Li, Z.-H., Gerya, T., Xu, Z.-Q., and Shi, Y.-L., 2018, Dynamics of terrane accretion during seaward continental drifting and oceanic subduction: Numerical modeling and implications for the Jurassic crustal growth of the Lhasa Terrane, Tibet: Tectonophysics, v. 746, p. 212–228, https://doi.org/10.1016/j.tecto.2017.07.018.

Yonkee, A., 2005, Strain patterns within part of the Willard thrust sheet, Idaho-Wyoming-Utah thrust belt: Journal of Structural Geology, v. 27, p. 1315–1343, https://doi.org/10.1016/j.jsg.2004.06.014.

Yonkee, W.A., and Weil, A.B., 2015, Tectonic evolution of the Sevier and Laramide belts within the North American Cordillera orogenic system: Earth-Science Reviews, v. 150, p. 531–593, https://doi.org/10.1016/j.earscirev.2015.08.001.